

Research Center for Molecular-Scale Nanoscience

VIII-C Development of Organic Semiconductors for Molecular Thin-Film Devices

Organic light-emitting diodes (OLEDs) and organic field-effect transistors (OFETs) based on π -conjugated oligomers have been extensively studied as molecular thin-film devices. Organic semiconductors with low injection barriers and high mobilities are required for highly efficient OLEDs and OFETs. Radical cations or anions of an organic semiconductor have to be generated easily at the interface with an electrode (or a dielectric), and holes or electrons must move fast in the semiconducting layer. Compared with organic *p*-type semiconductors, organic *n*-type semiconductors for practical use are few and rather difficult to develop. Recently, we found that perfluorinated oligomers are efficient electron-transport materials for OLEDs.

VIII-C-1 Perfluoro-1,3,5-tris(*p*-Oligophenyl)benzenes: Amorphous Electron-Transport Materials with High Glass-Transition Temperature and High Electron Mobility

KOMATSU, Shingo; SAKAMOTO, Youichi;
SUZUKI, Toshiyasu; TOKITO, Shizuo¹
(¹NHK Sci. Tech. Res. Labs.)

[*J. Solid State Chem.* in press]

Perfluoro-1,3,5-tris(*p*-quaterphenyl)benzene (**PF-13Y**) and perfluoro-1,3,5-tris(*p*-quinquephenyl)benzene (**PF-16Y**) have been synthesized and characterized. They showed higher glass transition temperatures compared with perfluoro-1,3,5-tris(*p*-terphenyl)benzene (**PF-10Y**). Organic light-emitting diodes (OLEDs) were fabricated using these materials as the electron-transport layers. **PF-13Y** and **PF-16Y** are better electron-transporters than **PF-10Y**. The electron mobilities of **PF-10Y** and Alq₃ were measured by the time-of-flight technique. **PF-10Y** showed higher electron mobilities (10^{-4} cm²/Vs) and weaker electric field dependence compared with Alq₃.

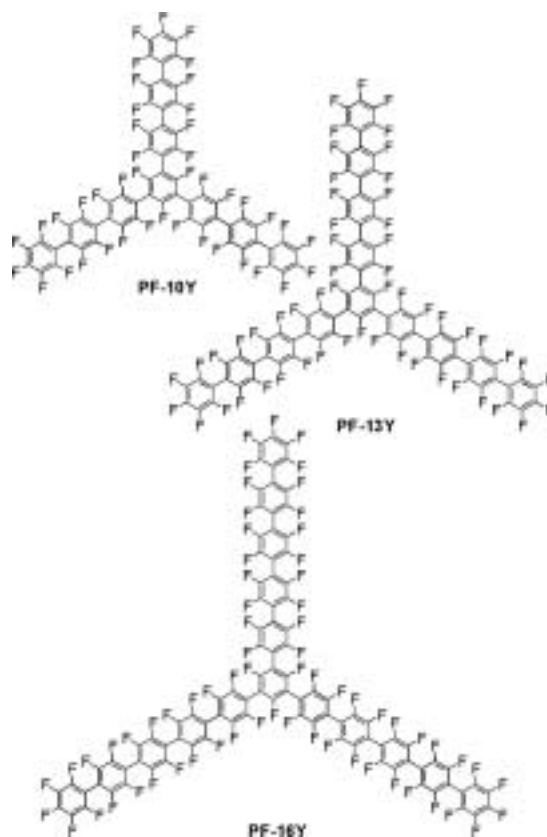


Figure 1. Perfluoro-1,3,5-tris(*p*-oligophenyl)benzenes.

VIII-C-2 Synthesis and Properties of Iridium Complexes Bearing Perfluoroaryl-Substituted 2-Phenylpyridine

SHIRASAWA, Nobuhiko; SAKAMOTO, Youichi;
SUZUKI, Toshiyasu; TSUZUKI, Toshimitsu¹;
TOKITO, Shizuo¹
(¹NHK Sci. Tech. Res. Labs.)

Perfluorophenyl derivatives of 2-phenylpyridine, 2-(*p*-C₆F₅-phenyl)pyridine (**1a**), 5-C₆F₅-2-phenylpyridine (**1b**), and 5-C₆F₅-2-(*p*-C₆F₅-phenyl)pyridine (**1c**), have been prepared. Their iridium(III) acetylacetonato complexes (**2a-c**) were satisfactorily synthesized in a one-pot reaction of a free ligand and an iridium salt in 2-ethoxyethanol at 105 °C, and the subsequent reaction

with acetylacetonate in the presence of a base at 50 °C for 4 h. When the reaction was carried out at 140 °C, the substitution reaction of fluoride with 2-ethoxyethoxide at para position took place. When applied to OLED devices, compounds **2a-c** showed emissions from greenish yellow to yellow at room temperature with the external quantum efficiency up to 14.7%.

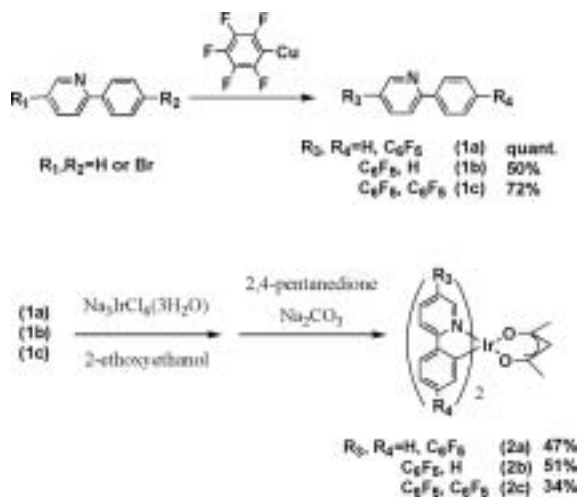


Figure 1. Synthesis of C_6F_5 -substituted ppy and their iridium acac derivatives.

VIII-D Field Effect Transistors with Organic Semiconductors

The mechanism of carrier transport in organic semiconductors and carrier injection from metal electrodes becomes the most important subject to be elucidated for the construction of high performance organic thin film devices. We have studied electrical properties of organic films using field effect transistors.

VIII-D-1 Electrical Characteristics of Phthalocyanine Films Prepared by Electrophoretic Deposition

TAKADA, Masaki¹; YOSHIOKA, Hirokazu²;
TADA, Hirokazu; MATSUSHIGE, Kazumi²
(¹GUAS; ²Kyoto Univ.)

[*Jpn. J. Appl. Phys.* **41**, L73 (2002)]

Electrical properties of phthalocyanine (Pc) films prepared by an electrochemical process were investigated using field effect transistors (FETs). Copper-Pc (CuPc) films were deposited electrophoretically on voltage-applied cathodic electrodes from trifluoroacetic acid/dichloromethane mixed solution containing protonated monomeric CuPc molecules. Optical absorption spectra showed that the CuPc films had α -type polymorphs. The grains grew with reaction time to close a gap between the FET electrodes. FET studies showed that CuPc films after annealing exhibited a *p*-type semiconducting behavior. Carrier mobility, conductivity and carrier density of the films were $1.4 \times 10^{-5} \text{ cm}^2/\text{Vs}$, $7.7 \times 10^{-7} \text{ S/cm}$ and $6.6 \times 10^{16} \text{ cm}^{-3}$, respectively. It is revealed that electrophoretic deposition is applicable for the preparation of active layers in organic electronic devices.

VIII-D-2 BTQBT (bis-(1,2,5-thiadiazolo)-*p*-Quinobis(1,3-dithiole)) Thin Films; A Promising Candidate for High Mobility Organic Transistors

TAKADA, Masaki¹; GRAAF, Harald;
YAMASHITA, Yoshiro²; TADA, Hirokazu
(¹GUAS, ²Tokyo Inst. Tech.)

[*Jpn. J. Appl. Phys.* **41**, L4 (2002)]

BTQBT (bis-(1,2,5-thiadiazolo)-*p*-quinobis(1,3-dithiole)) films have been prepared as active semiconducting layers of organic field effect transistors (FETs). BTQBT films showed a *p*-type semiconducting behavior. The hole mobility and on/off ratio of BTQBT films under ultrahigh vacuum conditions reached to $0.2 \text{ cm}^2/\text{Vs}$ and 10^8 , respectively, by optimization of the growth conditions. These values are in the same order as those of pentacene thin films, which indicates that BTQBT molecules have a great potential for active layers of organic electronic devices.

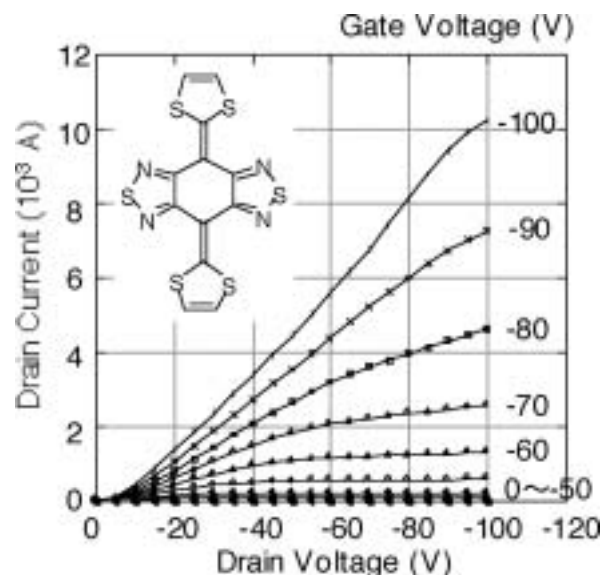


Figure 1. FET characteristics of BTQBT films measured in UHV.

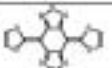
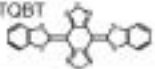
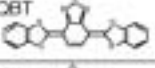
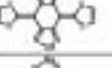
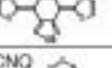
VIII-D-3 Field Effect Transistors of BTQBT and Its Derivatives

TAKADA, Masaki¹; YAMASHITA, Yoshiro²;
TADA, Hirokazu
(¹GUAS; ²Tokyo Inst. Tech.)

[*Proc. MRS 725*, P10.3 (2002)]

We have prepared and characterized thin film field effect transistors (FETs) of bis-(1, 2, 5- thiadiazolo)-*p*-quinobis(1, 3-dithiole) (BTQBT) and its derivatives. Preparation and characterization of the films were carried out under ultrahigh vacuum condition. Most materials examined showed *p*-type semiconducting behaviors. Among *p*-type molecules, BTQBT films deposited at room temperature showed *p*-type semiconducting behaviors with mobility of $0.1 \text{ cm}^2/\text{Vs}$. The on/off drain current ratio was 10^7 . The mobility and on/off ratio reached to $0.2 \text{ cm}^2/\text{Vs}$ and 10^8 , respectively, by optimizing the film growth conditions. These performances are almost comparable to those of pentacene and polythiophene thin films, indicated that BTQBT molecule is a prominent semiconducting material as a high mobility thin film. It was also found that tetracyanoquinodimethane (TCNQ) derivative showed an *n*-type semiconducting behavior with an electron mobility of $8.9 \times 10^{-4} \text{ cm}^2/\text{Vs}$.

Table 1. Field Effect Mobilities of BTQBT and Its Derivatives.

	type	Mobility(cm ² /Vs)	On/off ratio
BTQBT 	p	1.0×10^{-1} (0.2 at 50°C)	10^7
DB-BTQBT 	p	4.6×10^{-4}	10^4
DB-TQBT 	p	1.6×10^{-5}	50
TBQBT 	p	1.2×10^{-3}	3
BSQBT 	p	1.3×10^{-6}	10
BTDA-TCNQ 	n	8.9×10^{-4} Al electrodes	10^2

VIII-D-4 Preparation of Nanometer-Gap Electrodes for Field Effect Transistors by Electroplating

YAMADA, Ryo; TAKADA, Masaki¹; OISHI, Osamu; TADA, Hirokazu
(¹GUAS)

A pair of electrodes with a nanometer-scale spacing

was fabricated by electroplating of gold onto micrometer gap electrodes prepared through conventional photolithography. The electrodes were prepared on SiO₂ formed on a heavily doped Si substrate which serves as a gate electrode. Figure 1 shows a SEM micrograph of the electrode fabricated by this method. It was shown that the drain current changed as a function of a gate voltage when Ti-phthalocyanine thin film was deposited onto this electrode. Thus, the electrode made by this method can be used for the study of organic thin film field effect transistors.

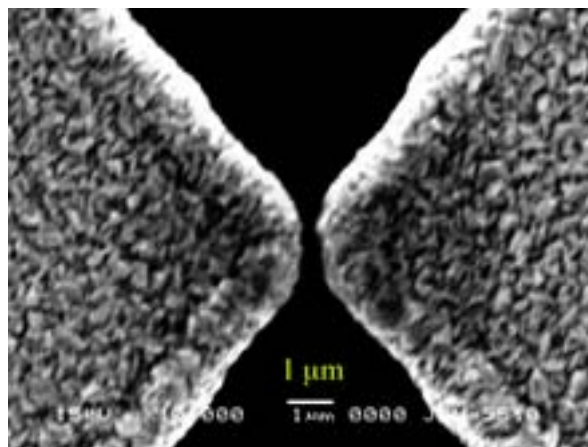


Figure 1. SEM Photograph of Nanometer Gap Electrodes.

VIII-E Preparation and Characterization of Highly Ordered Molecular Films on Silicon Bound with Si-C Covalent Bond

Self-assembled monolayers (SAMs) have received considerable attention because of their potential applications to molecular scale electronic devices. Covalently bond alkane SAMs formed by reaction between alkene and hydrogen terminated silicon are of increasing interest as nano-interface for molecular electronics devices fabricated on silicon microstructures. We have studied the growth manner and electronic structure of Si-C junction using scanning probe microscope such as STM (scanning tunneling microscope), AFM (atomic force microscope) and KFM (Kelvin force microscope).

VIII-E-1 Force Curve Measurement of Self-Assembled Organic Monolayers Bound Covalently on Silicon(111)

GRAAF, Harald; ARA, Masato¹; TADA, Hirokazu
(¹GUAS)

[*Mol. Cryst. Liq. Cryst.* **377**, 33 (2002)]

Self-assembled monolayers of alkyl chains were prepared on silicon(111) surfaces. The surface was characterized by atomic force microscopy (AFM). Atomically flat terraces were observed in topographic images of the films with contact mode AFM, indicating the formation of highly ordered monolayers. Force curve measurements showed that the adhesion force between organic films and gold cantilever was much stronger comparing to the force on hydrogen terminated

surfaces.

VIII-E-2 Atomic Force Microscope Anodization of Si(111) Covered with Alkyl Monolayers

ARA, Masato¹; GRAAF, Harald; TADA, Hirokazu
(¹GUAS)

[*Jpn. J. Appl. Phys.* **41**, 4894 (2002)]

Alkyl monolayers on Si were prepared through the reaction between 1-alkenes and hydrogen-terminated Si by heat treatment. The monolayers were characterized by atomic force microscopy (AFM), force curve and water contact angle measurements. It was found that surface properties were modified by the formation of highly ordered closely packed monolayers. The monolayers were anodized with a contact-mode AFM

by applying voltage between the conductive cantilever and surface under ambient conditions, which resulted in nanometer-scale oxidation of surfaces. After anodization, patterned areas were modified by removing the silicon oxide and terminating the surface of the grooves with hydrogen atoms by NH_4F etching, and by covering the etched surface with 1-octadecene molecules. The monolayers themselves showed high resistance to NH_4F etching and air oxidation.

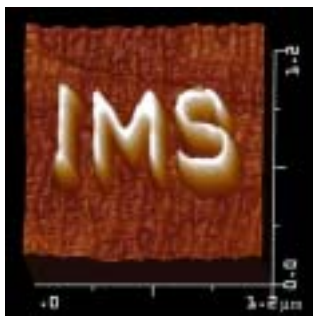


Figure 1. AFM anodization of Silicon Surfaces with AFM.

VIII-E-3 Nanopatterning of Alkyl Monolayers Covalently Bound to Si(111) with an Atomic Force Microscope

ARA, Masato¹; GRAAF, Harald; TADA, Hirokazu
(¹GUAS)

[*Appl. Phys. Lett.* **80**, 2565 (2002)]

Alkyl monolayers covalently bound to silicon were prepared through the reaction between 1-alkene molecules and hydrogen-terminated Si. The surfaces were anodized in nanometer scale with a contact-mode atomic force microscope (AFM) by applying positive bias voltage to the surface with respect to a conducting cantilever under ambient conditions. Following the anodization, patterned areas were selectively modified by chemical etching and coating with different molecules. The alkyl monolayers showed high resistance against chemical etching and protected Si surfaces from oxidation. AFM lithography of monolayers on Si was found to be useful for nanofabrication of organic/-inorganic interfaces based on the Si-C covalent bond.

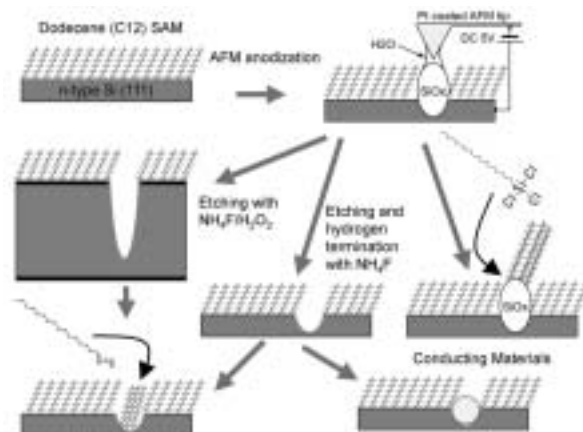


Figure 1. Nanopatterning of Silicon Surfaces with AFM.

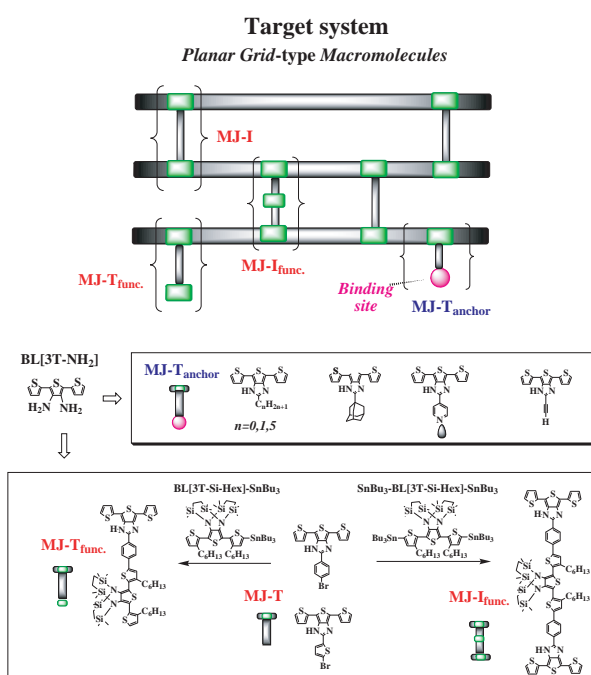
VIII-F Development of Precisely-Defined Macromolecules and their Organization on Substrate Surfaces for Molecular-Scale Electronics Circuits

The concept of molecular-scale electronics is now realized for individual components such as wire, diode, switch, and memory cell, but the fabrication of complete molecular-scale circuits remains challenging because of the difficulty of connecting molecular modules to one another. Molecular monolithic technology, which integrates the wiring, transistors and the required passive elements on a single macromolecule, has been proposed as a promising solution to this problem. In this project we have been trying to establish both the architecture of this novel class of macromolecules and the protocols for their purposive organization on metal/semiconductor substrate surfaces.

VIII-F-1 Design and Synthesis of Molecular Junction and Anchor Modules for Multi-Function Integrated Macromolecules

TANAKA, Shoji; YOKOYAMA, Takashi¹
(¹NIMS)

The design of “planar and multi-function integrated” π -conjugated macromolecules has been a subject of intensive research in the field of molecular electronics, because of their potential applications as basic components for future IT hardware such as ultra-dense molecular-scale quantum computers. In order to establish the architecture for this class of tailor-made macromolecules, we have developed various types of molecular building blocks and characterized them on substrate surfaces based on the high-resolution STM experiments combined with their bulk-level properties. Here we describe the synthesis of i) “molecule-anchor modules” for setting the molecular systems on metal/semiconductor substrate, and ii) “molecule-junction modules” for constructing planar grid-type molecular frameworks. Scheme 1 shows the synthetic pathways to these modules. Purification of these molecules was achieved by gel permeation chromatography. The purity of the obtained compounds was clearly revealed by MALDI-TOF mass spectroscopy using dithranol as matrix.



Scheme 1.

VIII-G Development of Novel Heterocyclic Compounds and their Molecular Assemblies for Advanced Materials

Heterocycles containing sulfur and/or nitrogen atoms are useful as components of functional materials since heteroatoms in their rings are helpful to stabilize ions or ion-radical species, and extended π -conjugation decreases Coulombic repulsion. In addition intermolecular interactions caused by heteroatom contacts can be expected to form novel molecular assemblies. In this project new electron acceptors, donors, and donor-acceptor compounds based on heterocycles such as 1,2,5-thiadiazole and 1,3-dithiole were synthesized and their properties including those of the charge-transfer complexes or ion-radical salts were investigated. Unique crystal structures were constructed by using weak intermolecular interactions such as hydrogen bonding or heteroatom contacts.

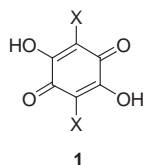
VIII-G-1 Crystal Engineering Using Anilic Acids and Dipyridyl Compounds through a New Supramolecular Synthron

ZAMAN, Md. Badruz¹; TOMURA, Masaaki;
YAMASHITA, Yoshiro²
(¹IMS and Steacie Inst. Mol. Sci.; ²IMS and Tokyo Inst.

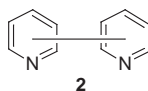
Tech.)

[*J. Org. Chem.* **66**, 5987 (2001)]

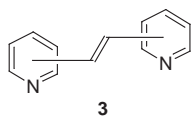
The anilic acids, 2,5-dihydroxy-1,4-benzoquinone **1a**, 2,5-dibromo-3,6-dihydroxy-1,4-benzoquinone (bromanilic acid; **1b**), 2,5-dichloro-3,6-dihydroxy-1,4-benzoquinone (chloranilic acid; **1c**), and 2,5-dicyano-3,6-dihydroxy-1,4-benzoquinone (cyananilic acid; **1d**), were cocrystallized with rigid organic ligands containing two pyridine rings, 2,4-bipyridine **2a**, 4,4'-bipyridine **2b**, 1,2-bis(2-pyridyl)ethylene **3a**, 1,2-bis(4-pyridyl)ethylene **3b**, 2,2'-dipyridylacetylene **4a**, 3,3'-dipyridylacetylene **4b**, and 4,4'-dipyridylacetylene **4c**. Fourteen complexes **5–18** were obtained as single crystals, and their crystal structures were successfully determined by X-ray analysis. All complexes except those with **2a** are 1 : 1 and are composed of an infinite linear or zigzag tape structure, the formation of which is ascribed to intermolecular O–H...N, N⁺–H...O, or N⁺–H...O[–] hydrogen bonds or a combination of these between the anilic acids and the dipyrindyl compounds. In the complexes **5** and **6**, no infinite tape structure is observed although the molecular units connected by a similar hydrogen-bonding pattern are formed. For the 1 : 1 complexes, we have found two types of stacking arrangements, segregated stacks (**7**, **9**, **12–15**, **18**) and alternated ones (**8**, **10**, **11**, **16**, **17**). In the complexes of **1c** with the series of dipyrindylacetylenes **4** (**14**, **15**, **17**), the neutral, dication, and monocation states are formed depending on the nitrogen positions, which can be attributed to the different basicity of the pyridyl groups.



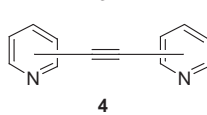
- 1a**: X = H
1b: X = Br
1c: X = Cl
1d: X = CN



- 2a**: 2,4-bipyridine
2b: 4,4'-bipyridine



- 3a**: 1,2-bis(2-pyridyl)ethylene
3b: 1,2-bis(4-pyridyl)ethylene



- 4a**: 2,2'-dipyridylacetylene
4b: 3,3'-dipyridylacetylene
4c: 4,4'-dipyridylacetylene

- 5**: complex between **1b** and **2a** **12**: complex between **1a** and **4c**
6: complex between **1c** and **2a** **13**: complex between **1b** and **4a**
7: complex between **1a** and **2b** **14**: complex between **1c** and **4a**
8: complex between **1c** and **2b** **15**: complex between **1c** and **4b**
9: complex between **1c** and **3a** **16**: complex between **1b** and **4c**
10: complex between **1b** and **3b** **17**: complex between **1c** and **4c**
11: complex between **1c** and **3b** **18**: complex between **1d** and **4c**

VIII-G-2 Bis(tetra-*n*-butylammonium) Bis(2-dicyanomethylene-4,5-dimercapto-1,3-dithiole)nickel(II)

TOMURA, Masaaki; YAMASHITA, Yoshiro¹(¹IMS and Tokyo Inst. Tech.)[*Acta Crystallogr., Sect. E* **58**, m133 (2002)]

We have carried out the X-ray crystallographic analysis of the title dithiolato-nickel complex derived from 2-dicyanomethylene-4,5-dimercapto-1,3-dithiole (dcndmdt) ligand.¹ This ligand in the nickel complex has peripheral heteroatoms and extended π -conjugated systems. In the nickel complex, [Ni(dcndmdt)₂](*n*-Bu₄N)₂, the centrosymmetric dianion is flat. The nickel atom has square-planar coordination, with Ni–S bond lengths of 2.1836(16) and 2.1940(18) Å.

Reference

- 1) M. Tomura and Y. Yamashita, *J. Mater. Chem.* **5**, 1753 (1995).

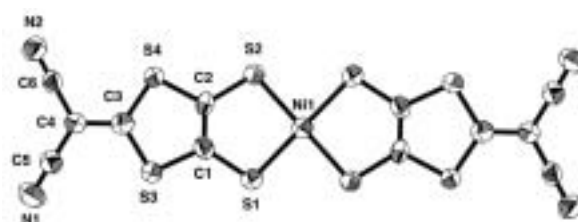


Figure 1. Molecular structure of the dianion in [Ni(dcndmdt)₂](*n*-Bu₄N)₂.

VIII-G-3 ¹H NMR Analysis and Crystal Structures of 1,1',3,3'-Tetramethyl-2,2'-bi-1*H*-Imidazolium Bis(tetraphenylborate): Ion-Associative Interactions Containing Ketone, Aldehyde, and Nitrile

ONO, Katsuhiko¹; SAITO, Katsuhiko¹; UCHIUMI, Hideki¹; TOMURA, Masaaki
 (¹Nagoya Inst. Tech.)

[*Chem. Lett.* 622 (2002)]

According to ¹H NMR analysis of 1,1',3,3'-tetramethyl-2,2'-bi-1*H*-imidazolium bis(tetraphenylborate) **1** in acetone and acetonitrile, high magnetic field shifts of the chemical shifts were observed. The facts are ascribable to ion association between the biimidazolium dication and BPh₄ anions. The crystals of **1** included some kinds of ketone, aldehyde, and nitrile as guest molecules to afford unique molecular aggregations. The biimidazolium dication is surrounded by four BPh₄ anions and is in a specific cyclic environment arising from eight phenyl groups, as shown in Figure 1. The molecular arrangements of the biimidazolium dication in the crystals can be controlled by the guest molecules.

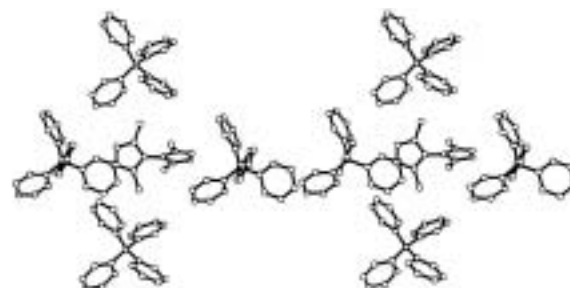


Figure 1. Stereo view of the packing mode of **1**-cyclohexanone.

VIII-G-4 4,7-Diiodo-2,1,3-Benzothiadiazole and 7,7'-Diiodo-4,4'-bis(2,1,3-benzothiadiazole)

TOMURA, Masaaki; AKHTARUZZAMAN, Md.¹; SUZUKI, Kazuharu²; YAMASHITA, Yoshiro³
(¹GUAS; ²IMS and Inst. Res. Innov.; ³IMS and Tokyo Inst. Tech.)

[*Acta Crystallogr., Sect. C: Cryst. Struct. Commun.* **58**, o373 (2002)]

The title compounds, 4,7-diiodo-2,1,3-benzothiadiazole **1** and 7,7'-diiodo-4,4'-bis(2,1,3-benzothiadiazole) **2** crystallize in the $P2_1/a$ and the noncentrosymmetric $Fdd2$ space group, respectively. In the crystal structures of **1**, a large number of short S...N and I...I contacts, and a planar I_4 square cluster are observed, as shown in Figure 1. The angle between the planes for the two 2,1,3-benzothiadiazole rings of **2** is $48.4(1)^\circ$, and short and linear N...I contacts [$3.333(8)$ Å] exist in the crystal of **2**.

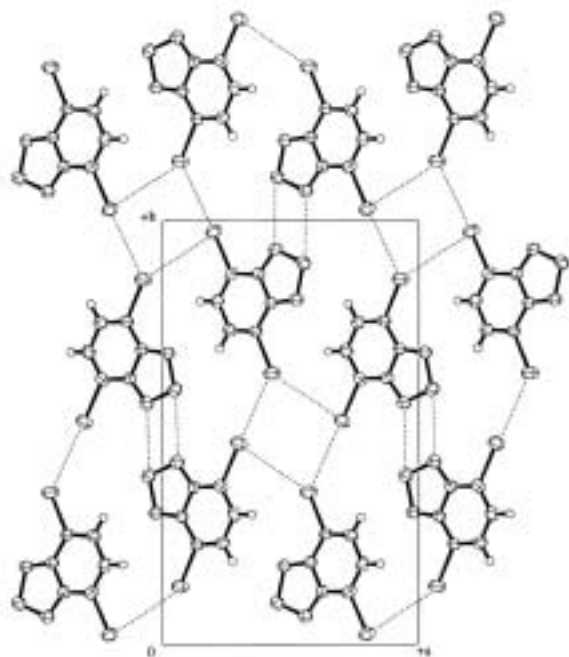


Figure 1. Packing diagram of **1** viewed along the c axis. Dotted lines show the short S...N and I...I contacts.

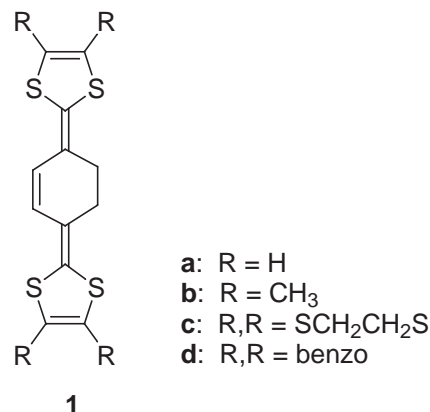
VIII-G-5 Synthesis and Properties of π -Extended TTF Analogues and Their Cation Radical and Dication Salts

YAMASHITA, Yoshiro¹; TOMURA, Masaaki; URUICHI, Mikio; YAKUSHI, Kyuya
(¹IMS and Tokyo Inst. Tech.)

[*Mol. Cryst. Liq. Cryst.* **376**, 19 (2002)]

New bis(1,3-dithole) electron donor **1** containing a cyclohexene unit were prepared using a Wittig-Honer reaction and a cycloreversion reaction. The tetramethyl

derivative afforded the highly conductive cation radical salts as single crystal whose unusual crystal structures were revealed by X-ray crystallographic analysis.



VIII-G-6 Synthesis and Structure of Bi- and Terthiophene Derivatives Having 4-Pyridylethynyl Substituents

TOMURA, Masaaki; YAMASHITA, Yoshiro¹
(¹IMS and Tokyo Inst. Tech.)

Conjugated organic oligomers are gaining increasing attention as new and promising materials in the field of molecular electronics. We have synthesized the title compounds, which are able to coordinate with metals and perform intermolecular interaction *via* hydrogen bonding, using the Sonogashira reaction. The X-ray crystallographic analyses of them revealed that the centrosymmetric bithiophene derivative has the *anti* conformation, whereas the crystallographically independent terthiophene derivative has *anti-cis* conformation. All thiophene and pyridine rings in the two derivatives are almost coplanar.

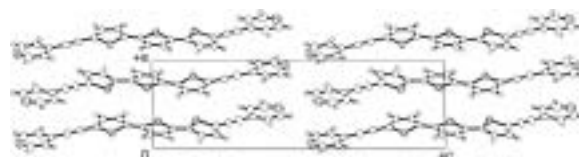


Figure 1. Molecular packing of 5,5''-bis[(4-pyridyl)ethynyl]-2,2':5',2''-terthiophene viewed along the b axis.

VIII-H Designing Artificial Photosynthesis at Molecular Dimensions

Photosynthesis is one of the finest piece of molecular machinery that Nature has ever created. Its ultrafast electron transfer and following well-organized sequence of chemical transformation have been, and will continue to be, challenging goals for molecular scientists. We are trying to mimic the function of photosynthesis by assembling molecular units that perform individual physical/chemical action. The molecular units include porphyrins, redox active organic molecules, and transition metal complexes. Our ultimate goal is to design artificial molecular systems that effect multiple chemical reactions triggered by light on the basis of molecular rationale.

VIII-H-1 Photoinduced Oxidation of Alcohols Catalyzed by Porphyrins and TEMPO

ITO, Hajime; NAGATA, Toshi

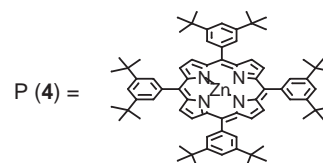
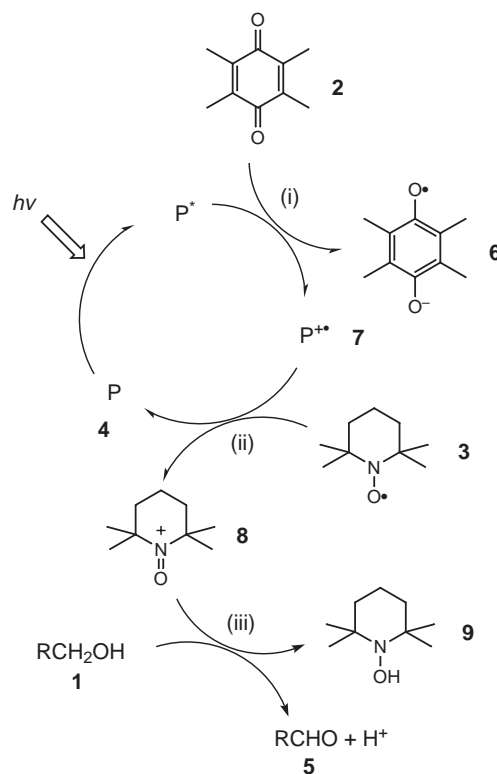
Photoinduced electron transfers involving porphyrins are widely studied, but utilizing the high-energy radical ion pairs for driving chemical reactions remains to be a great challenge. Herein we report the TEMPO-mediated oxidation of alcohols catalyzed by porphyrins under irradiation with visible light. Although there have been many reports on TEMPO-mediated oxidation of alcohols, our system is the first to utilize photoinduced electron transfer including porphyrins.

When a solution of benzyl alcohol (**1**, 0.1 mmol), duroquinone (**2**, 0.1 mmol), TEMPO (**3**, 2,2,6,6-tetramethylpiperidine N-oxide, 0.1 mmol), diisopropylethylamine (0.2 mmol) and 5,10,15,20-tetrakis(3,5-*di-t*-butylphenyl)porphinatozinc(II) (**4**, 0.001 mmol) in THF/DMF (1/1, 0.5 ml) was irradiated with visible light ($\lambda > 500$ nm, halogen lamp with a Toshiba Y-52 filter) for 10 hours, benzaldehyde (**5**) was formed in 23% yield. On addition of tetrabutylammonium perchlorate (0.1 mmol), the yield was improved to 42%. When either TEMPO, duroquinone, diisopropylethylamine or porphyrin was omitted, or in the absence of light, no benzaldehyde was detected.

As the reaction proceeded, 2,2,6,6-tetramethyl-N-hydroxypiperidine (TEMPO-H, **9**) was detected together with benzaldehyde, indicating that the oxidant was TEMPO rather than duroquinone. It is noteworthy, however, that in the absence of duroquinone the reaction did not proceed. The role of duroquinone is rationally understood by assuming photoinduced electron transfer from the porphyrin to the quinone. The tentative reaction mechanism is shown in Scheme 1; (i) the photoexcited porphyrin transfers an electron to the quinone, (ii) the cation radical of the porphyrin (**7**) oxidizes TEMPO to give the oxoammonium intermediate (**8**), (iii) the oxoammonium cation oxidizes the alcohol (**1**) with the aid of the base. The quinone anion radical (**6**) should be oxidized to regenerate the quinone either (iv) by the porphyrin cation radical, (v) by the oxoammonium cation, or (vi) by TEMPO. As the paths (iv) and (v) are non-productive, they result in the lower efficiency. Indeed, the reaction was too slow to be synthetically useful, so that we looked into the way to improve the reaction efficiency.

A moderate success was achieved by changing the electron acceptor. When 2,6-*di-t*-butyl-1,4-benzoquinone was used in place of duroquinone, benzalde-

hyde was obtained in 86% yield by use of 0.2 equivalents of TEMPO instead of the stoichiometric amount (solvent = base = pyridine, 27 hours irradiation). In this system, 2,5-*di-t*-butyl-1,4-hydroquinone accumulated instead of TEMPO-H. We assume that direct oxidation of the quinone anion radical was suppressed by the introduction of the bulky *t*-butyl groups.



Scheme 1.

VIII-I Development of New Metal Complexes as Redox Catalysts

Redox catalysis is an important field of chemistry which translates a flow of electron into chemical transformation. It is also one of the requisites for artificial photosynthesis. This project of ours aims at developing new metal complexes that perform redox catalysis at low overpotential. We have been focusing our attention to developing terdentate ligands with strong donor character, and have found that introducing a pyrrole ligand in place of pyridine leads to useful ligands.

VIII-I-1 Syntheses of a 6-(2-Pyrrolyl)-2,2'-Bipyridine Derivative and Its Ruthenium Complex

NAGATA, Toshi; TANAKA, Koji

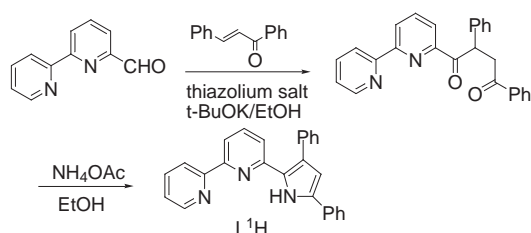
[*Bull. Chem. Soc. Jpn.* in press.]

Metal complexes of pyrroles are gathering interest as an activator of the pyrrole ring, an intermediate for synthesizing pyrrole derivatives, and as a component of conducting polymers. Herein we report the syntheses of 6-(3,5-diphenyl-2-pyrrolyl)-2,2'-bipyridine (L^1H) and its ruthenium complex $[Ru(L^1)_2]$. The compound L^1H is the first example of the "ter-aryl" ligand that has one pyrrole and two pyridine rings in this order, and it will be a useful substitute for 2,2':6',2''-terpyridine (terpy) when more electron-donating character is desirable.

The synthesis of L^1H is shown in Scheme 1. The Stetter condensation of 2,2'-bipyridine-6-carbaldehyde with chalcone was utilized, followed by ring closure of the 1,4-diketone with an ammonium salt (67% yield). By use of pyridine-2,6-dicarbaldehyde as a starting material, the compound L^2H_2 , 2,6-bis(3,5-diphenyl-2-pyrrolyl)pyridine, was also obtained (69% yield).

The ORTEP drawing of the complex $[Ru(L^1)_2]$ is shown in Figure 1. The coordination geometry around the Ru(II) center is similar to that of $[Ru(terpy)_2]X_2$, however the six pyridine/pyrrole rings are not exactly coplanar.

The cyclic voltammograms of $[Ru(L^1)_2]$ and $[Ru(terpy)_2](ClO_4)_2$ are shown in Figure 2. The Ru(III)/Ru(II) couple appeared at -0.29 V (*versus* ferrocene/ferrocenium couple) in $[Ru(L^1)_2]$, which was 1.10 V more negative than in $[Ru(terpy)_2](ClO_4)_2$, consistent with the strong donor character of the L^1 ligand. The first reduction wave (reduction of the ligand) was also negatively shifted by 0.51 V. At higher potential range ($+0.5$ – 0.7 V), $[Ru(L^1)_2]$ showed irreversible waves suggesting the oxidative degradation of the complex. Apparently the oxidation of the pyrrole rings led to the degradation of the ligand and/or the decomplexation of the metal ion.



Scheme 1. Synthesis of the ligand L^1H .

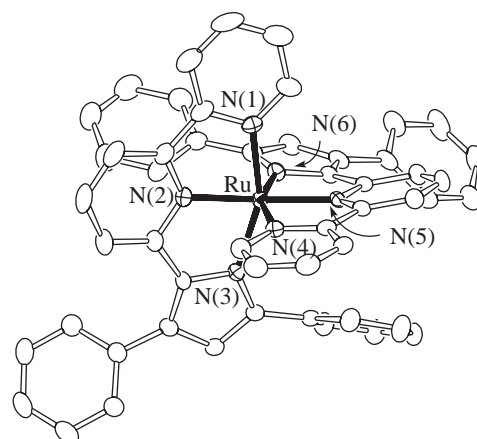


Figure 1. ORTEP view (50% probability ellipsoids) of the complex $[Ru(L^1)_2]$.

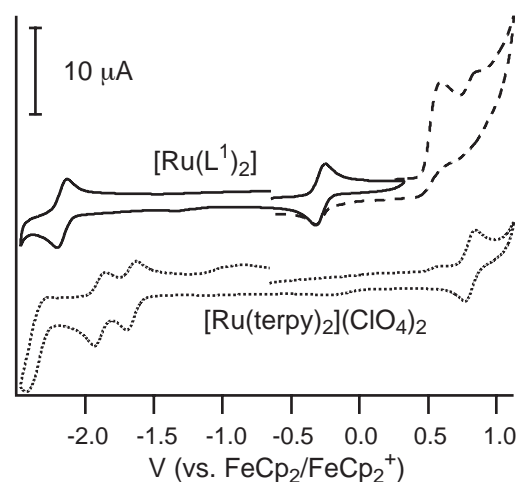


Figure 2. The cyclic voltammograms of $[Ru(L^1)_2]$ and $[Ru(terpy)_2](ClO_4)_2$.

VIII-J Electronic Properties of Monolayer-Protected Metal Clusters

Monolayer-protected metal clusters or nanoparticles have received much attention recently because their electronic and optical properties can be tuned by their sizes and shapes. The novel electronic properties of the clusters as well as their tunability are important from the viewpoint of future application as optoelectronic nanodevices. Our interests are focused on the following topics on the thiol-derivatized metal clusters and nanoparticles: (1) preparation and characterization of small clusters with core diameters of ~ 1 nm range (~ 40 atoms/cluster) which may exhibit molecular-like electronic and charging properties, (2) determination of structural dimensions (core diameters and monolayer thickness) of metal nanoparticles, and (3) development of size-selection method for the clusters and nanoparticles. Our goal is to reveal the evolution of electronic structures of the metal clusters as a function of the cluster size.

VIII-J-1 Development of Mass Spectrometer for Clusters

NEGISHI, Yuichi; TSUKUDA, Tatsuya

Mass spectrometry provides detailed informations on the chemical compositions of the metal clusters. We have constructed a time-of-flight (TOF) mass spectrometer which accommodates three types of ion sources: (1) a matrix-associated laser desorption ionization (MALDI) source for clusters obtained as solid, (2) an electrospray ionization source for clusters dispersed in aqueous phase, and (3) an electron-impact ionization source for molecular clusters. Only a brief description on the MALDI/TOF apparatus, which has been developed recently, is presented here. The specimens for mass analysis are prepared by depositing an aliquot (~ 1–5 μL) of the mix solutions of cluster samples and matrix onto a surface of a target made of stainless steel. After the solvent is evaporated at ambient atmosphere, the target is fed into the mass spectrometer through a load-lock chamber and attached to one of acceleration grids. The sample is irradiated with the third harmonic (355 nm) of a Nd:YAG laser operated at 10 Hz. The laser fluence is adjusted typically in the range of 10–40 $\mu\text{J}/\text{mm}^2/\text{pulse}$. The cluster ions thus formed are accelerated by applying a pulsed high voltage (15–20 kV) to the electrode plates. The ion beams are focused and stirred by ion optics and then detected by a MCP detector located at the end of the flight path of 1.17 m. Mass spectra of the ions of either polarity can be recorded by simply changing the polarities of the power supplies.

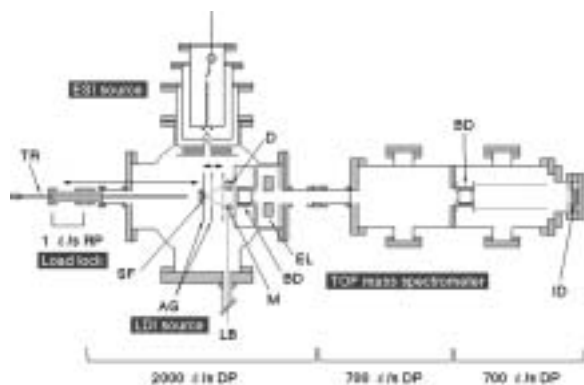


Figure 1. Schematic diagram of the apparatus: TR: transfer rod, SF: sample folder, AG: acceleration grid, LB: laser beam, M: mirror, D: damper, BD, beam deflectors, EL: einzel lens, ID: ion detector. Details of the ESI source are not described here. The EI source installed perpendicularly to the diagram is not shown.

VIII-J-2 Formation of $\text{Pd}_n(\text{SR})_m$ Clusters ($n < 60$) in the Reactions of PdCl_2 and RSH ($\text{R} = n\text{-C}_{18}\text{H}_{37}$, $n\text{-C}_{12}\text{H}_{25}$)

NEGISHI, Yuichi; MURAYAMA, Haruno; TSUKUDA, Tatsuya

[*Chem. Phys. Lett.* **366**, 561 (2002)]

Mass spectroscopic analysis revealed that Pd clusters passivated by thiolates as well as the stoichiometric thiolate complexes $\text{Pd}_n(\text{SR})_{2n}$ ($n = 5, 6$) are formed in the reactions between palladium chloride and n -alkane-thiols (RSH: $\text{R} = n\text{-C}_{18}\text{H}_{37}$, $n\text{-C}_{12}\text{H}_{25}$) in toluene. The Pd clusters thus formed are formulated as $\text{Pd}_n(\text{SR})_m$ with $m \sim 0.6n$ and the cluster size are distributed in the range of $5 \leq n \leq 60$, being consistent with core diameters of ~ 1 nm determined by TEM observations. A gap of ~ 2 eV was observed in the optical transition of the $\text{Pd}_n(\text{SR})_m$ clusters showing the emergence of non-metallic properties as a result of the size reduction.

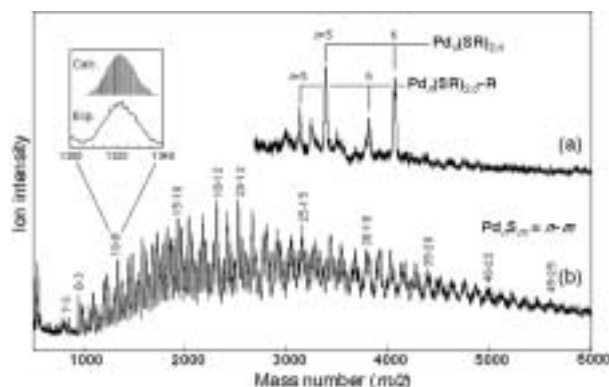


Figure 1. Typical representations of MALDI mass spectra of the mixtures of $\text{PdCl}_2/n\text{-C}_{18}\text{H}_{37}\text{SH}$ which are diluted with anthracene to (a) ~ 1 and (b) ~ 20 mol%.

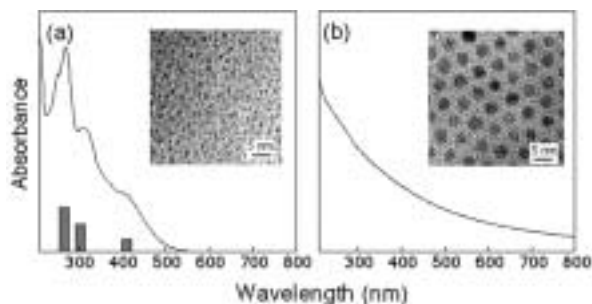


Figure 2. Optical spectra of hexane solutions of (a) PdCl₂/*n*-C₁₈H₃₇SH mixture and (b) Pd:SC₁₈H₃₇ nanoparticles. The solid bars in panel (a) represent the absorbance of the Pd_{*n*}(SC₁₈H₃₇)_{2*n*} complexes (*n* = 5 and 6).

VIII-J-3 Size-Selective Preparation of Water-Soluble Gold Clusters

NEGISHI, Yuichi; TSUKUDA, Tatsuya

Colloidal solution of gold clusters was formed upon mixing AuCl or AuCl₄⁻ and *meso*-dimercaptosuccinic acid (DMSA: HO₂CCH(SH)CH(SH)CO₂H) in water. The size distributions of the gold clusters can be controlled by simply changing the mixing ratios of the gold salts and DMSA as revealed by optical spectroscopy and TEM observations. Figure 1 shows the uv-vis spectra of the colloidal solutions prepared with different mixing ratios between AuCl and DMSA. With increase in the ratios of DMSA, the surface plasmon band at ~530 nm disappears and the onset of the optical transition shifts toward shorter wavelength, implying the reduction of the cluster sizes. The TEM measurements confirm this trend: the average sizes of the Au cores are 3.1 ± 0.7 and 1.8 ± 0.6 for the mixing ratios [DMSA]/[AuCl] of 1 and 2, respectively (Figure 2). These findings indicate the DMSA molecules act both as reducing agents against the Au(I) or Au(III) ions and stabilizing ligands for the resulting Au(0) clusters. Optimization of preparation conditions as well as purification of the clusters by polyacrylamide gel electrophoresis (PAGE) and gel permeation chromatography (GPC) is now under way in our laboratory.

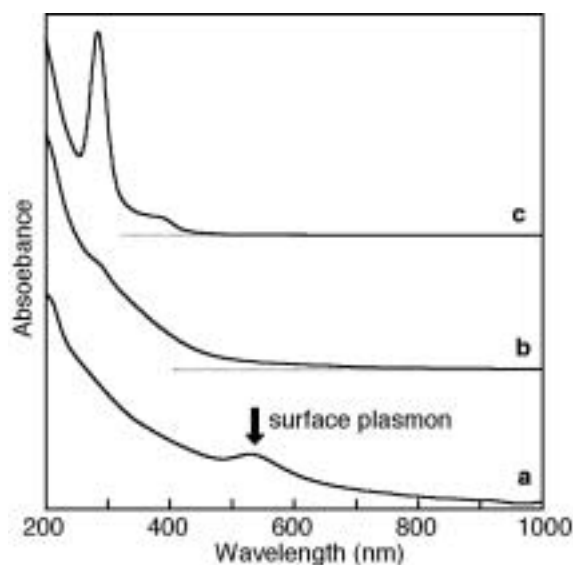


Figure 1. Optical spectra of colloidal solutions of gold clusters prepared with the mixing ratios [DMSA]/[AuCl] of (a) 0.1, (b) 0.2, and (c) 0.4.

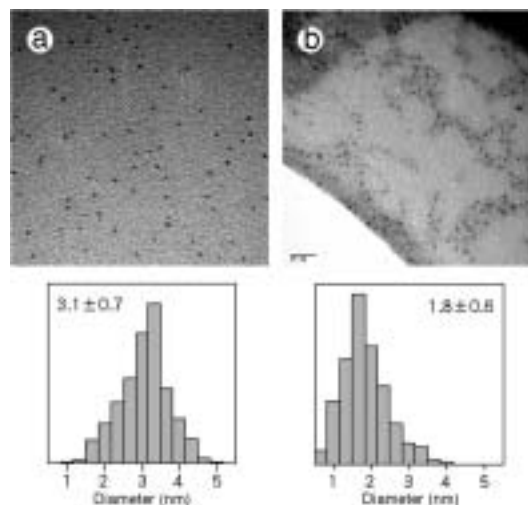


Figure 2. TEM images and size distributions of gold clusters obtained with the mixing ratios [DMSA]/[AuCl] of (a) 1 and (b) 2.

VIII-J-4 Characterization and Purification of Pd:SR Nanoparticles by Gel Permeation Chromatography

MURAYAMA, Haruno; TSUKUDA, Tatsuya

Gel permeation chromatography (GPC) and transmission electron microscopy (TEM) have been used to characterize the structures of Pd:SR (R = *n*-C₁₈H₃₇, C₁₆H₃₃, C₁₄H₂₉, C₁₂H₂₅, C₁₀H₂₁, C₆H₁₃) nanoparticles. The Pd:SR nanoparticles are prepared by ligand exchange of PVP-protected Pd nanoparticles.¹⁾ The difference between the average diameter (*D_c*) measured by TEM and hydrodynamic diameter (*D_h*) determined by GPC allows us to determine the thickness (*T*) of the monolayer of alkanethiolates. On the basis of these results together with the length of free alkanethiols, a structural model of the monolayers on the Pd clusters has been proposed. It is also demonstrated that the Pd:SR clusters which are size selected by GPC show pronounced tendency to self-assemble into two-dimensional superlattices (Figure 1). Further purification of the clusters by the GPC in a recycled mode is now in progress in our group.

Reference

- 1) T. Tsukuda, N. Kimura, T. Sasaki and T. Nagata, *Trans. Matr. Res. Soc. Jpn.* **25**, 929 (2000).

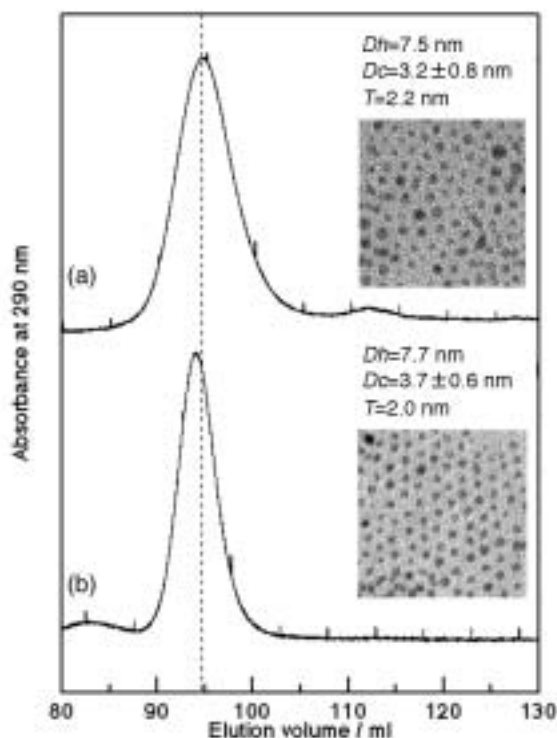


Figure 1. Chromatograms and TEM images for (a) as-prepared and (b) purified Pd:SR nanoparticles.

VIII-K Structures and Dynamics of Molecular Cluster Ions

Molecular clusters, intermediate states of matter between bulk and a molecule, provide us unique opportunities to study how the chemical and physical properties evolve with a degree of aggregation. We studied photo-induced reactions within size-selected cluster anions and evolutions of crystal structures of clusters.

VIII-K-1 Structural Evolution of Large $(\text{CO}_2)_n^-$ Clusters as Studied by Mass Spectrometry

NEGISHI, Yuichi; NAGATA, Takashi¹; TSUKUDA, Tatsuya
(¹Univ. Tokyo)

[*Chem. Phys. Lett.* **364**, 127 (2002)]

The mass distributions of $(\text{CO}_2)_n^-$ produced by electron-impact ionization of a free jet have been measured up to $n \sim 10^3$. Several intensity anomalies observed in a small size range are ascribed to the stabilities of the negative ions. In contrast, a series of humps are clearly discernible in the range of $n \geq 100$, which reflects the abundance of neutral $(\text{CO}_2)_n$. The intensity oscillations are analyzed in the context of “geometrical shell closings.” The analysis reveals that the $(\text{CO}_2)_n$ clusters with $n > \sim 80$ have truncated forms of an *fcc* crystal, most likely a cuboctahedral motif (Figure 1).

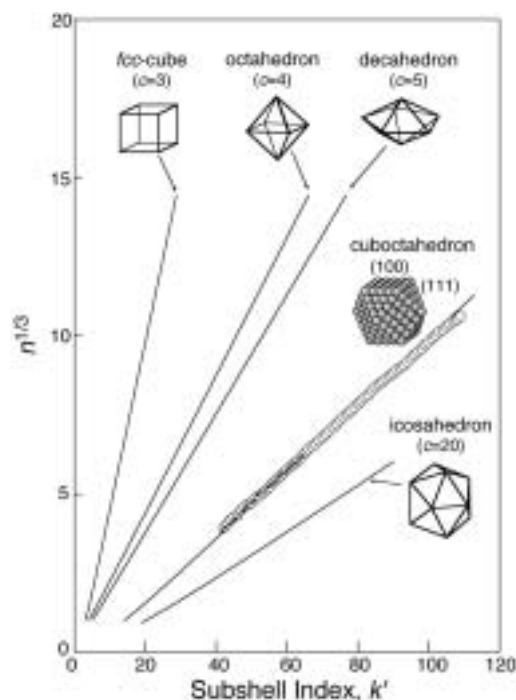


Figure 1. Plots of $n^{1/3}$ against the subshell index k' for various polyhedra. Symbols \circ and \bullet represent the experimental data for $(\text{CO}_2)_n^-$ and $(\text{CO}_2)_n^+$, respectively. Both plots are explicable in terms of cuboctahedra (CO). The spheres in the CO motif represent the CO_2 constituent molecules.

VIII-K-2 Photochemistry of $(\text{NO})_n^-$ as Studied by Photofragment Mass Spectrometry

TSUKUDA, Tatsuya; ZHU, Lei¹; SAEKI, Morihisa; NAGATA, Takashi²

(¹Data Storage Inst.; ²Univ. Tokyo)

[*Int. J. Mass Specrom.* **220**, 137 (2002)]

Photofragmentation of $(\text{NO})_n^-$ ($3 \leq n \leq 21$) in the energy range 2.7–3.6 eV (350–460 nm) results in the production of $(\text{NO})_m^-$ with $m \geq 2$ and $\text{NO}_2^-(\text{NO})_m$ with $0 \leq m \leq 2$. The photofragment yield spectra obtained for $n = 3-7$ display a broad and structureless band profile with successive blue-shift with increase in the cluster size, indicating that N_3O_3^- (reference 1) behaves as a chromophoric core in the larger $(\text{NO})_n^-$. The observed fragmentation patterns suggest that photoexcitation of the N_3O_3^- chromophore is followed by direct dissociation into $(\text{NO})_2^-$, solvent evaporation to form $(\text{NO})_m^-$, and/or intracluster reactions to produce NO_2^- .

Reference

1) T. Tsukuda, M. Saeki, L. Zhu and T. Nagata, *Chem. Phys. Lett.* **295**, 416 (1998).

VIII-L Rotational Echo Double Resonance (REDOR) Experiments with Overtone Adiabatic Inversion Pulses

The effect of an overtone adiabatic inversion pulse on solid-state ^{14}N spins was investigated.

VIII-L-1 The Observation of REDOR Phenomena for Solid-State ^{13}C - ^{14}N Spin Systems with the Help of Overtone Adiabatic Inversion Pulses

KUWAHARA, Daisuke

We applied overtone adiabatic inversion pulses to ^{13}C - ^{14}N spin systems in powdered *L*-alanine undergoing MAS in order to observe REDOR phenomena. The damping of ^{13}C resonance line intensities was compared with that corresponding to the REDOR experiments with normal RF pulses having a constant frequency. We tried to establish the theoretical treatment for the REDOR experiments with adiabatic inversion pulses. The computer simulations for the REDOR experiments revealed that overtone adiabatic pulses had little dependence on the offsets of rf carrier frequencies.

VIII-M Nanoscale Characterization of Heterogeneous Catalyst Surfaces

Heterogeneous catalysis occurs on a surface of a solid catalyst. Active centers for heterogeneous catalysis commonly consist of clusters of several surface atoms, and thus a long-range order of surface atoms is not normally required. Therefore, when using precious metals as catalysts, nanometer-scale superfine particles are commonly employed in order to increase its surface area and to decrease the amount of catalysts. This introduces difficulties in characterizing the catalyst surfaces and their active centers, because characterization techniques of solid surfaces at nanometer-scale are not well established. Here we mainly used scanning probe microscopes, in conjunction with other surface characterization techniques, to characterize catalytically active centers as well as the nature of catalyst-support interactions.

VIII-M-1 Determination of Extra-Framework Cation Positions and Their Occupancies on Heulandite(010) by Atomic Force Microscopy

KOMIYAMA, Masaharu; GU, Minming¹; WU, Hai-Ming²
(¹McGill Univ.; ²Res. Inst. Innovative Tech. Earth)

[*J. Phys. Chem. B* **105**, 4680 (2001)]

Atomic images of a cleaved heulandite(010) surface were obtained under an aqueous condition by atomic force microscopy (AFM). In addition to the framework oxygen atoms on the (010) plane, extra-framework cations on the surface were also imaged. An AFM imaging simulation was performed using published X-ray diffraction data to assist the assignment of the AFM-observed framework and extra-framework atoms. By comparing it with the observed AFM images, local variations of position and occupancy of individual cations were determined.

VIII-M-2 Molecular Orbital Interpretation of Thymine/Graphite NC-AFM Images

KOMIYAMA, Masaharu; UCHIHASHI, Takayuki¹; SUGAWARA, Yasuhiro^{1,2}; MORITA, Seizo²
(¹Joint Res. Center Atom Tech.; ²Osaka Univ.)

[*Surf. Interface Anal.* **29**, 53 (2001)]

Recent non-contact atomic force microscopy (nc-AFM) images of a deoxyribonucleic acid (DNA) base thymine (2,4-dioxy-5-methylpyrimidine), vacuum-deposited on a highly-oriented pyrolytic graphite (HOPG) surface, are interpreted by means of theoretical adsorption simulations, and the molecular geometry and the energetics of the adsorption system are estimated. The lowest-energy dimer configuration was found to be the one in which the respective hydrogen on number 1 nitrogen and oxygen on number 6 carbon of two thymine molecules make a hydrogen bond to each other. A surface unit cell structure was reproduced. Adsorption energy for the thymine pair on HOPG is rather small, amounting to only *ca.* 1 kcal/mol, with small variations depending on the molecular orientation with respect to the substrate surface. A possibility of having a mirrored adsorption configuration in adjacent domains is also suggested.

VIII-M-3 Partial Reduction of Si(IV) in SiO₂ Thin Film by Deposited Metal Particles—An XPS Study

KOMIYAMA, Masaharu; SHIMAGUCHI, Takemi¹
(¹Yamanashi Univ.)

[*Surf. Interface Anal.* **29**, 189 (2001)]

Metal-support interactions in the systems of dispersed metals supported on thin film silica surfaces were examined by X-ray photoelectron spectroscopy. Four metal-silica systems, Pt-, Pd-, Ag- and Au-SiO₂, all indicated the formation of partially reduced Si(IV) species by the metal deposition. The extent of the reduction varied little with the kind and the amount of deposited metal species. On the other hand, the amount of this newly formed Si(IV-δ) indicated a strong metal species dependence.

VIII-M-4 Apparent Local Structural Change Caused by Ultraviolet Light on a TiO₂ Surface Observed by Scanning Tunneling Microscopy

KOMIYAMA, Masaharu; YIN, Donghong¹
(¹Hunan Normal Univ.)

[*Jpn. J. Appl. Phys.* **40**, 4281 (2001)]

An apparent local surface structural change at nanoscale was observed by scanning tunneling microscopy on a TiO₂ surface upon irradiation with ultraviolet (UV) light. This phenomenon was reversible with UV light irradiation, and was interpreted to be due to the local accumulation of photoexcited states. This is the first real-space observation of inhomogeneous local charge distribution under UV light irradiation at nanoscale on a semiconductive photocatalyst surface, which may help identify the photocatalytic active sites and elucidate their reaction mechanisms.

VIII-M-5 Various Phases on Natural Stilbite (010) Surface Observed by Atomic Force Microscopy under Aqueous Conditions

GU, Ning¹; KOMIYAMA, Masaharu
(¹Southeast Univ.)

[*Jpn. J. Appl. Phys.* **40**, 4285 (2001)]

Various phases on a natural stilbite (010) surface were observed by atomic force microscopy (AFM) under aqueous conditions. In a wide-area observation, oriented protrusions observed on the surface differed from the “sheaflike” structure which has been found in stilbite in an aqueous NaOH solution. Narrow-area observations showed surfaces consisting of an island structure, or a structure of alternating ridges and trenches. The latter is similar to the one reported previously under ambient conditions. The atomically resolved AFM image of the stilbite confirms that its surface is in good agreement with the known crystallographic parameters of the bulk-terminated (010) surface. Defects such as dislocations and grain boundaries at the atomic level were also observed.

VIII-N Studies of Electronic Structure of Organic Thin Films and Organic/Inorganic Interfaces by Electron Spectroscopies

Electronic structures of organic film surface and organic/inorganic interface are expected to play an important role in organic-device properties. We investigated surface structures and energy alignments to clarify their electronic structures using surface sensitive spectroscopy such as photoelectron spectroscopy combined with synchrotron radiation and metastable atom electron spectroscopy.

VIII-N-1 Low Energy Electron Diffraction of the System In-[perylene-3,4,9,10-tetracarboxylic Dianhydride] on MoS₂

AZUMA, Yasushi¹; IWASAKI, Kazuaki²;
KURIHARA, Tsutomu²; OKUDAIRA K., Koji;
HARADA, Yoshiya³; UENO, Nobuo¹
(¹IMS and Chiba Univ.; ²Chiba Univ.; ³Seitoku Univ.)

[*J. Appl. Phys.* **91**, 5024 (2002)]

The system In-perylene-3,4,9,10-tetracarboxylic dianhydride ~PTCDA on MoS₂, prepared by the sequential evaporation of PTCDA and In on a cleaved MoS₂ surface, was studied by low energy electron diffraction. The result indicates that reaction products form an ordered structure on the MoS₂ surface. From the analysis of the diffraction pattern, the presence of six symmetry-equivalent domains of an oblique unit cell of In-PTCDA species results with the dimensions of 9.5 Å, 16.3 Å, and an enclosed angle of 80.2°. In addition, splitting in two domains by a mirror plane exists with the rotation angle $R5610.8^\circ$ with respect to each of the three equivalent surface crystal axes of the MoS₂ substrate. The new structure is explained by assuming that four In atoms are chemically bonded to the four carbonyl groups of the PTCDA molecules. Furthermore, it is concluded that the In₄PTCDA species become tilted after a chemical reaction between the PTCDA molecules and the In atoms, which is in agreement with results previously obtained by angle-resolved ultraviolet photoemission experiments.

VIII-N-2 Electronic Structure and Molecular Orientation at Thin Film Surfaces of Pendant-Group Polymers Studied by Outermost Surface Spectroscopy Using Metastable Atoms

OKUDAIRA K., Koji; KERA, Satoshi²;
SETOYAMA, Hiroyuki²; MORIKAWA, Eiji³;
UENO, Nobuo¹
(¹IMS and Chiba Univ.; ²Chiba Univ.; ³Louisiana State Univ.)

[*J. Electron Spectrosc. Relat. Phenom.* **121**, 225(2001)]

Metastable-atom electron spectroscopy (MAES) and ultraviolet photoelectron spectroscopy (UPS) were used to study the outermost surface of thin films of pendant group polymers: polystyrene (PSt), poly(2-vinylnaphthalene), and poly(9-vinylcarbazole). MAES is selectively sensitive to the outermost surface, and indicated that the surfaces of the polymer films were very clean,

even though they were prepared by spin-casting in a room atmosphere. In Figure 1 observed MAES and UPS of PSt are shown. By comparison with gas-phase spectra and molecular orbital calculations of model molecules with pendant groups, it was confirmed that the principal constituent at the outermost surface of these polymer films is the pendant groups. Furthermore, it was observed that the intensity for σ (C-H) states of the pendant group is stronger in MAES spectra than in UPS spectra, indicating many pendant groups are inclined at large tilt angles.

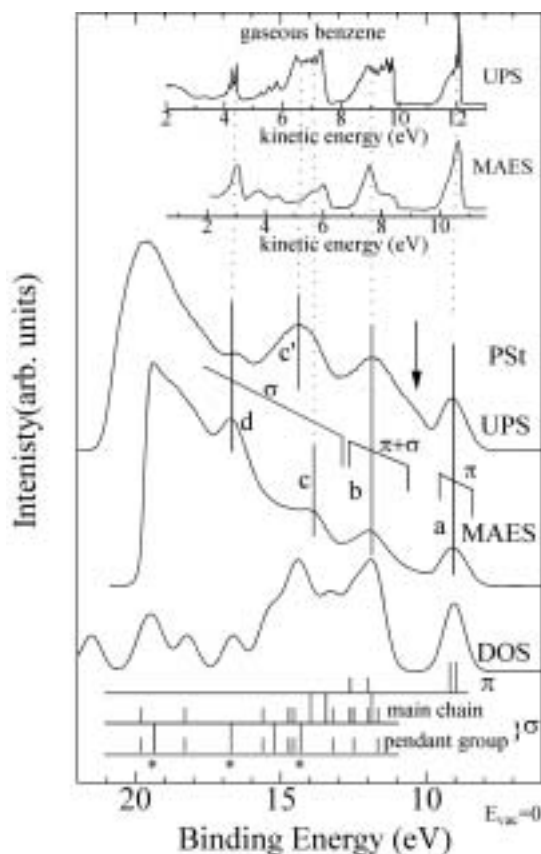


Figure 1. MAES and UPS of polystyrene (PSt) thin film. The vertical bars show the molecular orbital energies calculated by *ab initio* MO calculation (6-31G with diffuse function) for the model compound of PSt. The energy levels for the molecular orbital consisted of π orbital at pendant group and σ orbital at polymer chain are represented by the vertical bars marked by asterisk(*). The density of states (DOS) was obtained by broadening with gaussian function (width = 0.8 eV). The calculated binding energy scale was contracted by 1.35 and shifted to fit with the experimental results. The inset shows the MAES and UPS of gaseous benzene.

VIII-N-3 Photodegradation of Poly(tetrafluoroethylene) and Poly(vinylidene fluoride) Thin Films by Inner Shell Excitation

OKUDAIRA K., Koji; YAMANE, Hiroyuki²; ITO, Kazuhiko²; IMAMURA, Motoyasu³; HASEGAWA, Shinji; UENO, Nobuo¹
(¹IMS and Chiba Univ.; ²Chiba Univ.; ³AIST)

[*Surf. Rev. Lett.* **9**, 335 (2002)]

Ion time-of-flight (TOF) mass spectra of poly(tetrafluoroethylene) (PTFE) and poly(vinylidene fluoride) (PVDF) thin films near fluorine and carbon *K*-edges were observed. For PTFE thin films peaks corresponding to F^+ , CF^+ , and CF_3^+ appeared, while for PVDF F^+ and H^+ were mainly observed. They indicate that for PTFE the polymer chain (C–C bonds) as well as C–F bonds are broken by irradiation of photons near fluorine and carbon *K*-edges, while for PVDF the bond scission occurs mainly at the C–F and C–H bond. Partial ion yields (PIY) of these ions for PTFE and PVDF thin films show strong photon energy dependencies near fluorine (Figure 1) and carbon *K*-edges. The excitation from fluorine $1s$ to $\sigma(C-F)^*$ is specially efficient for F^+ ion production for both PTFE and PVDF.

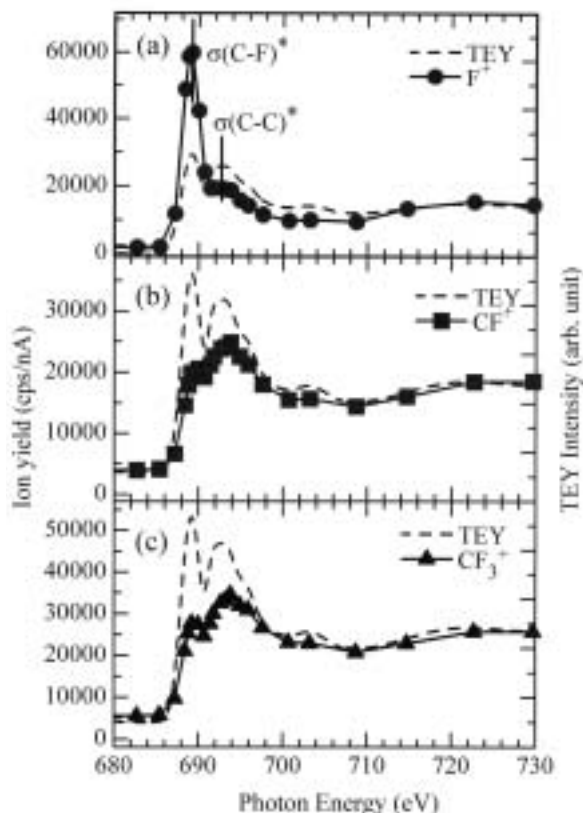


Figure 1. PIY spectra of (a) F^+ , (b) CF^+ and (c) CF_3^+ for PTFE thin film near the fluorine *K* absorption edge. TEY spectra (broken curve) are also shown for comparison. TEY spectra are renormalized at $h\nu = 682.5$ eV and at $h\nu = 730$ eV to fit PIY intensities.

VIII-N-4 Intramolecular Energy-Band Dispersion in Oriented Thin Film of n - $CF_3(CF_2)_{22}CF_3$ Observed by Angle-Resolved UV Photoemission and its Theoretical Simulation

YOSHIMURA, Daisuke¹; ISHII, Hisao²; MIYAMAE, Takayuki³; HASEGAWA, Shinji⁴; OKUDAIRA K., Koji⁵; UENO, Nobuo; SEKI, Kazuhiko¹
(¹Nagoya Univ.; ²Tohoku Univ.; ³AIST; ⁴Fuji Xerox; ⁵Chiba Univ.)

[*Surf. Rev. Lett.* **9**, 407 (2002)]

Poly(tetrafluoroethylene) (PTFE) $(CF_2)_n$ is one of the most fundamental polymers, which is the perfluorinated analogue of polyethylene $(CH_2)_n$ with a simple repeating CF_2 unit. For such a one-dimensional polymer, we can expect the formation of one-dimensional intramolecular energy-band relation along the chain direction, and the energy-band structures of PTFE have been studied theoretically. Unfortunately, however, there was no experimental result to be compared with such calculated energy-band structure. In this work, we performed angle-resolved UV photoemission spectroscopy (ARUPS) with synchrotron radiation for the oriented thin films of perfluorotetracosane (n - $CF_3(CF_2)_{22}CF_3$; PFT), which is one of the oligomer of PTFE. The sample of PFT with their long chain axis being perpendicular to the surface was prepared by in-situ vacuum evaporation. The normal-emission spectra of the PFT film show incident photon energy dependence due to the intramolecular energy-band dispersion. We also performed the theoretical simulation of the spectra by using independent-atomic-center (IAC) approximation combined with *ab initio* MO calculations. The simulations successfully reproduced the $h\nu$ -dependence of the observed ARUPS spectra. From the observed and simulated spectra, we deduced the value of inner potential V_0 , which is the parameter defining the energy origin of the free-electron-like final state, and derived reliable energy-band dispersion relation.

VIII-O Study on Compact X-Ray Sources

Electron storage rings are useful and practical devices as x-ray sources. However, these synchrotron radiation facilities which can provide intense x-rays usually occupy large area and we need many costs in order to construct and maintain the facilities. So that there have been many works to investigate compact x-ray sources. Laser undulator radiation and backward Compton scattering which are generated by interaction of electron beams from small accelerators with intense laser photons are candidates to produce hard x-rays.

X-ray sources must be shielded for radiation safety. For constructing effective shields, we need to know how many radiations are yielded from our x-ray sources. We will use high energy electrons to produce x-rays. These electrons cause radiations when they interact with beam ducts or beam dumps, so that it is useful to study radiations generated in synchrotron radiation facilities in order to estimate the yields of radiations from our x-ray sources.

VIII-O-1 Study on Radiation Shielding for Small Synchrotron Radiation Facilities

TAKASHIMA, Yoshifumi; KUWAYAMA, Shunsuke¹; KOBAYAKAWA, Hisashi¹
(¹Nagoya Univ.)

X-ray sources using high energy electrons usually generate radiations which should be shielded. In order to design effective shields, we need to estimate how many radiations are generated from a storage ring and penetrate radiation shields. Circulating electrons in a storage ring go out of their stable orbit when their energy exceeds the critical energy. These electrons are incident on the beam duct and generate electromagnetic showers around the beam duct.

We measured angular distribution of radiations around a beam duct of the storage ring of UVSOR. Figure 1 shows experimental set up. Two Photodiodes were set in tandem in a copper case and coincident signal from these two photodiodes were counted, so that we detected only charged particles. The area of the photodiodes were $7 \times 7 \text{ mm}^2$. We used 12 pairs of photodiodes installed at about 2 m upstream from the inflector. Figure 2 shows an angular distribution of the number of signal from the detectors. We notice that the stray radiations of charged particles counted at inside of the ring are more than that counted at outside, because most electrons which exceed their energy over the bucket height hit on the inside wall of the beam duct.

In order to estimate the amount of the stray radiations around compact x-ray sources, we should investigate the spatial distribution of stray radiations by comparing experimental results and theoretical calculations. We will propose a simple formula to calculate radiation dose around a small accelerator. In order to check the accuracy of the formula, we should measure the radiations at many points around UVSOR storage ring and compare the experimental results with our calculations.

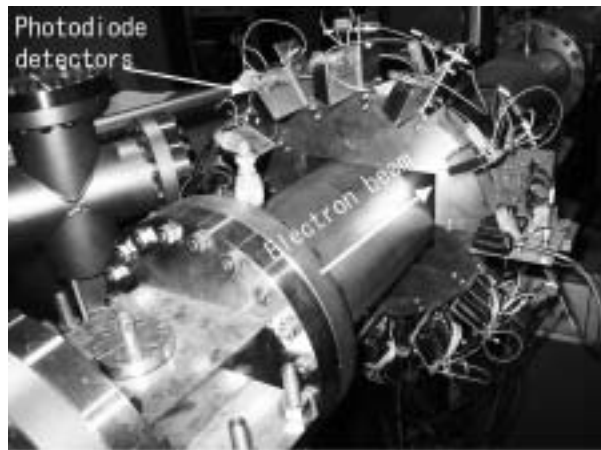


Figure 1. Experimental setup.

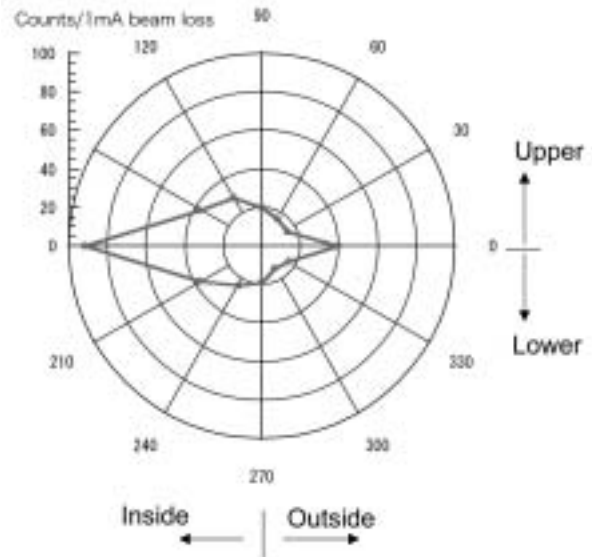


Figure 2. Angular distribution of charged particles around the beam duct of the storage ring of UVSOR.

VIII-P Syntheses of Fullerene-Based New Materials with Novel Physical Properties

Fullerene-based new materials are synthesized, and the structures and physical properties are studied in wide temperature and pressure regions. The structures and transport properties of pressure-induced superconducting fulleride, Cs_3C_{60} , are studied by X-ray powder diffraction, ESR, Raman, AC susceptibility and resistivity measurements, in order to clarify the mechanism of pressure-induced superconductivity. The structures and transport properties of metallofullerenes are also studied by X-ray diffraction and resistivity. The field-effect transistors (FET's) with thin-films of fullerenes are fabricated and their transport properties are studied in wide temperature region. STM studies on metallofullerenes adsorbed on Si(111)-(7×7) surface are performed under high vacuum condition.

VIII-P-1 Pressure and Temperature Dependences of the Structural Properties of Dy@C₈₂ Isomer I

TAKABAYASHI, Yasuhiro¹; KUBOZONO, Yoshihiro; KANBARA, Takayoshi¹; FUJIKI, Satoshi; SHIBATA, Kana²; HARUYAMA, Yusuke²; HOSOKAWA, Tomoko²; RIKIISHI, Yoshie²; KASHINO, Setuo²
(¹IMS and Okayama Univ.; ²Okayama Univ.)

[*Phys. Rev. B* **65**, 73405 (2002)]

Crystals of Dy@C₈₂ isomer I are studied by x-ray powder diffraction with synchrotron radiation in wide temperature and pressure regions. The isomer I of Dy@C₈₂ shows a simple cubic structure with lattice constant, a , of 15.85(3) Å at 298 K, while the isomer II shows a face-centered cubic structure with a of 15.75(4) Å. The structural phase transition of the second-order is indicated for the isomer I at 300–310 K by the temperature dependence of x-ray diffraction and differential scanning calorimetry. Further, the pressure dependence of the lattice constant is studied for the isomer I up to 60 kbar, which can be fitted by a Murnaghan equation of state.

VIII-P-2 Ferromagnetism and Giant Magnetoresistance in the Rare-Earth Fullerides Eu_{6-x}Sr_xC₆₀

ISHII, Kenji^{1,2}; FUJIWARA, Akihiko¹; SUEMATSU, Hiroyoshi¹; KUBOZONO, Yoshihiro
(¹Univ. Tokyo; ²JAERI)

[*Phys. Rev. B* **65**, 134431 (2002)]

We have studied crystal structure, magnetism, and electric transport properties of a europium fulleride Eu₆C₆₀ and its Sr-substituted compounds, Eu_{6-x}Sr_xC₆₀. They have a *bcc* structure, which is an isostructure of other $M_6\text{C}_{60}$ (M represents an alkali atom or an alkaline-earth atom). Magnetic measurements revealed that magnetic moment is ascribed to the divalent europium atom with $S = 7/2$ spin, and a ferromagnetic transition was observed at $T_c = 10$ –14 K. In Eu₆C₆₀, we also confirm the ferromagnetic transition by heat-capacity measurement. The striking feature in Eu_{6-x}Sr_xC₆₀ is very large negative magnetoresistance at low tempera-

ture; the resistivity ratio $\rho(H = 9 \text{ T})/\rho(H = 0 \text{ T})$ reaches almost 10^{-3} at 1 K in Eu₆C₆₀. Such large magnetoresistance is the manifestation of a strong π - f interaction between conduction carriers on C₆₀ and $4f$ electrons of Eu.

VIII-P-3 Bridging Fullerenes with Metals

CHI, Dam Hieu¹; IWASA, Yoshihiro^{1,2,3}; CHEN, X. H.⁴; TAKENOBU, Taishi²; ITO, Takayoshi¹; MITANI, Tadaoki¹; NISHIBORI, Eiji⁵; TAKATA, Masaki⁵; SAKATA, Makoto⁵; KUBOZONO, Yoshihiro
(¹JAIST; ²Tohoku Univ.; ³CREST; ⁴Univ. Sci. Tech. China; ⁵Nagoya Univ.)

[*Chem. Phys. Lett.* **359**, 177 (2002)]

The bonding nature between rare earth metals and fullerene molecules has been investigated. The electron density distribution for nominal Sm₃C₇₀, calculated by a maximum entropy method (MEM) based on the Rietveld analysis of synchrotron X-ray diffraction pattern, unambiguously demonstrated a covalent Sm...C bond, which is almost as strong as the interatomic bonding of crystal Si. Furthermore, the Sm bridges two C₇₀ molecules, producing a C₇₀...Sm...C₇₀ dimer structure.

VIII-P-4 Structure and Physical Properties of Cs_{3+α}C₆₀ (α = 0.0–1.0) under Ambient and High Pressures

FUJIKI, Satoshi; KUBOZONO, Yoshihiro; KOBAYASHI, Mototada²; KAMBE, Takashi¹; RIKIISHI, Yoshie¹; KASHINO, Setuo¹; ISHII, Kenji³; SUEMATSU, Hiroyoshi³; FUJIWARA, Akihiko⁴
(¹Okayama Univ.; ²Himeji Inst. Tech.; ³Univ. Tokyo; ⁴JAIST)

[*Phys. Rev. B* **65**, 235425 (2002)]

The intermediate phases, Cs_{3+α}C₆₀ (α = 0.0–1.0), have been prepared, and their structure and physical properties are studied by x-ray powder diffraction, Raman, ESR, electric conductivity and ac susceptibility measurements under ambient and high pressures. The x-ray powder diffraction pattern of Cs_{3+α}C₆₀ (α = 0.0–

1.0) can be indexed as a mixture of the body-centered-orthorhombic (*bco*) and cubic (A15) phases. The A15 phase diminishes above 30 kbar. The broad ESR peak due to conduction electron (*c*-ESR) is observed only for the phases around $\alpha = 0.0$ in $Cs_{3+\alpha}C_{60}$. The resistivity of the $Cs_{3+\alpha}C_{60}$ ($\alpha \neq 0$) sample follows the granular metal theory and/or Sheng model even in the sample exhibiting a broad ESR peak. No superconducting transition is observed up to 10.6 kbar in $Cs_{3+\alpha}C_{60}$ ($\alpha \neq 0$). These results present that *bco* phase of $Cs_{3+\alpha}C_{60}$ ($\alpha = 0$) is a final candidate for a pressure-induced superconductor.

VIII-P-5 Complex-Plane Impedance Study on a Hydrogen-Doped Copper Coordination Polymer: *N,N'*-bis-(2-hydroxy-ethyl)-Dithiooxamidato-Copper(II)

NAGAO, Yuki¹; IKEDA, Ryuichi¹; KANDA, Seiichi²; KUBOZONO, Yoshihiro; KITAGAWA, Hiroshi^{1,3,4}

(¹Univ. Tsukuba; ²Univ. Tokushima; ³JAIST; ⁴JST)

[*Mol. Cryst. Liq. Cryst.* **379**, 89 (2002)]

AC conductivity measurements with an impedance analyzer were carried out for a hydrogen-doped coordination polymer, *N,N'*-bis-(2-hydroxy-ethyl)-dithiooxamidato-copper(II), in order to estimate the protonic conductivity (σ_p). The $\log \sigma_p$ was linearly increased from 2.6×10^{-9} to 2.2×10^{-6} $S\text{cm}^{-1}$ with relative humidity (RH) from 45 to 100% at 300 K. A slight hysteresis of protonic conductivity was observed upon increasing and decreasing RH, which implies that H_3O^+ is generated by a reaction between water molecule and acid-base polymer near RH \sim 100%.

VIII-P-6 Crystal Structure and Electronic Transport of Dy@C₈₂

KUBOZONO, Yoshihiro; TAKABAYASHI, Yasuhiro¹; SHIBATA, Kana²; KANBARA, Takayoshi¹; FUJIKI, Satoshi; KASHINO, Setuo²; FUJIWARA, Akihiko³; EMURA, Shuichi⁴

(¹IMS and Okayama Univ.; ²Okayama Univ.; ³JAIST; ⁴Osaka Univ.)

[*Phys. Rev. B* submitted]

Crystal structure of Dy@C₈₂ isomer I at 298 K has been determined by Rietveld refinement for X-ray powder diffraction with synchrotron radiation. The isomer I shows a simple cubic structure (sc: $Pa\bar{3}$) with a lattice constant, *a*, of 15.78(1) Å. The C₂ axis of a C_{2v}-C₈₂ cage aligns along a [111] direction of this crystal lattice. The C₈₂ cage is orientationally disordered to satisfy a $\bar{3}$ symmetry along [111] which is requested in this space group. The large thermal parameter for the Dy atom estimated from the X-ray diffraction probably reflects a large disorder caused by a floating motion of the Dy atom inside the C₈₂ cage as well as a ratchet-type motion of the Dy@C₈₂ molecule. The electronic transport of thin film of Dy@C₈₂ shows a semi-conducting behavior. The energy gap, E_g , is estimated to

be 0.2 eV. Further, the variation of valence from Dy³⁺ to Dy²⁺ is found by metal-doping into the Dy@C₈₂ crystals.

VIII-P-7 N-Channel Field-Transistors with Thin Films of Fullerenes

KANBARA, Takayoshi²; FUJIKI, Satoshi²; SHIBATA, Kana¹; KUBOZONO, Yoshihiro¹; URISU, Tsuneo; SAKAI, Masahiro; FUJIWARA, Akihiko³

(¹Okayama Univ.; ²IMS and Okayama Univ.; ³JAIST)

[*Phys. Rev. B* submitted]

N-channel field effect transistors (FETs) are fabricated with thin films of C₆₀, C₇₀ and Dy@C₈₂, and an SiO₂ insulating layer. The transport properties of the C₆₀ and C₇₀ FET's are studied in a temperature region from 200 to 330 K. The typical FET properties are observed in C₆₀ and C₇₀ above 220 K. The hopping transport with activation energy of 0.3 eV is observed for the C₆₀ and C₇₀ FET's in this temperature region. Further, the condition of fabrication is studied in order to improve the FET property. The Dy@C₈₂ FET is first fabricated and its property is studied at 295 K.

VIII-P-8 STM Study of Dy@C₈₂ on Si(111)-(7×7) Surface

FUJIKI, Satoshi; KUBOZONO, Yoshihiro; KANBARA, Takayoshi¹; FUJIWARA, Akihiko²; HOSOKAWA, Tomoko¹; URISU, Tsuneo

(¹Okayama Univ.; ²JAIST)

[to be submitted]

Single-molecule image of Dy@C₈₂ on Si(111)-(7×7) surface is observed by STM. The Dy@C₈₂ molecules were deposited on the Si(111)-(7×7) surface under UHV chamber. The first layer of Dy@C₈₂ is disordered, and no second layer islands are found before the complete formation of the first layer of Dy@C₈₂. A single-molecule image of Dy@C₈₂ was clearly observed on the first layer. This image shows that the maximum height of the molecule is \sim 11.3 Å which corresponds to those of two long axes of Dy@C₈₂ inclusive of van der Waals radius of C atom. The STS of the multilayer of Dy@C₈₂ suggests a energy gap of 0.1 eV at 295 K, in consistent with that, 0.2 eV, determined by resistivity measurement for the Dy@C₈₂ thin film. This shows that the Dy@C₈₂ molecule is a small-gap semiconductor.

VIII-Q Effects of High Magnetic Field on Chemical Process

It is interesting to control chemical and physical process with the aid of magnetism which is one of the key properties of matter. This research group is studying the mechanisms of the interaction of matter and magnetic field in order to develop a new technique to control chemical and physical process by magnetic field. In the anodic oxidation reaction of potassium iodide, significant magnetic field effects (≤ 0.6 T) on the product yields are interpreted in terms of the Lorentz force on iodide ions. In the liquid/solid redox reaction of silver ion and copper metal, anomalous magnetic field effects (≤ 15 T) are chiefly explained by the magnetic force on generated copper ions. It is clarified that mass transportation in solution is remarkably affected by the magnetic field.

VIII-Q-1 Magnetic Field Effects on Anodic Oxidation of Potassium Iodide

UECHI, Ichiro¹; FUJIWARA, Masao¹; FUJIWARA, Yoshihisa²; YAMAMOTO, Yohsuke²; TANIMOTO, Yoshifumi¹

(¹IMS and Hiroshima Univ.; ²Hiroshima Univ.)

[*Bull. Chem. Soc. Jpn.* in press]

External magnetic fields (≤ 6 kG) significantly increase yields of I_3^- and H_2 as well as anodic currents in anodic oxidation of potassium iodide. At 0.7 V, the ratio of the current at 6 kG and at 0 kG is about 1.7, whereas that of I_3^- yield is 1.2. The ratio of the H_2 yield is 1.4 at 2 kG. The Lorentz force on ions in the solution induces convection of solution (MHD flow), resulting in acceleration of the entire reaction rate. The MHD flow of the solution is confirmed from the visual observation that reddish-brown streams of I_3^- in the solution, moving downward at zero field, undergo turbulent motion in magnetic fields. Small magnetic field effect on the I_3^- yield, compared to that on the anodic current, is attributable to the fact that the reaction of I_3^- and OH^- , generated at the cathode, is also enhanced by the MHD flow.

VIII-Q-2 High Magnetic Field Effect on the Growth of 3-Dimensional Silver Dendrites

KATSUKI, Akio¹; UECHI, Ichiro; FUJIWARA, Masao; TANIMOTO, Yoshifumi

(¹Shinshu Univ.)

[*Chem. Lett.* submitted]

A liquid/solid redox reaction between silver ion and copper metal is investigated under high vertical magnetic field (maximum field strength: 15 T). The magnetic field causes drastic changes in the color and shape of silver dendrites. At zero field, branches of metallic silver grow on the gray and cylindrical dendrites. In the presence of magnetic field, the dendrites are black in color and almost spherical in shape. The dendrites in magnetic field are denser than those at zero field. In the presence of the magnetic field, yields of silver dendrite and copper ion increase by 1.3–2. These effects are chiefly interpreted in terms of the magnetic force in copper ion in solution. As the reaction progresses, paramagnetic copper ions are generated. These ions are attracted by the magnetic force, leading to the convection of the solution.

VIII-R Theoretical and Computational Study on Gas Phase Reactions and Chromic Molecules

Quantum chemical calculations are used to produce potential energy surface (PES) to do reaction dynamics simulations. We develop the methodology to generate PES efficiently and/or automatically using quantum chemical calculation results. Another interest of our group is theoretical explanation and prediction of structural and spectral changes of photochromic and electrochromic substances.

VIII-R-1 Polycyano–Polycadmte Host Clathrates Including a Methylviologen Dication. Syntheses, Crystal Structures and Photo-Induced Reduction of Methylviologen Dication

YOSHIKAWA, Hirofumi¹; NISHIKIORI, Shin-ichi¹; WATANABE, Tokuko²; ISHIDA, Toshimasa³; WATANABE, Go³; MURAKAMI, Makoto³; SUWINSKA, Kinga⁴; LUBORADZKI, Roman⁴; LIPKOWSKI, Janusz⁴

(¹Univ. Tokyo; ²Tokyo Univ. Fisheries; ³Shizuoka Univ.; ⁴Polish Acad. Sci.)

[*J. Chem. Soc., Dalton Trans.* 1907 (2002)]

A series of polycyano-polycadmte host clathrates including a methylviologen dication (MV^{2+}), which is a photo-hemically active electron acceptor, and an organic molecule, such as alcohols, haloalkanes, ethers and small aromatics, and two complexes built of a polycyano-polycadmte and MV^{2+} were synthesized. The single crystal X-ray diffraction experiments on ten clathrates and the two complexes revealed their 3-D network polycyano-polycadmte structures built of Cd^{2+} ions and CN. bridges. The network structures are classified into five structure types. Type I, II and III were found in the clathrates, and Type IV and V were turned up in the two complexes. Type I and II have cage-like cavities and each of the cavities includes one guest, MV^{2+} or an organic molecule. Type III has a channel-like cavity where MV^{2+} ions and organic molecules are included. Type IV and V have 3-D space, which is neither a cage-like cavity nor a channel-like cavity, for embracing MV^{2+} . Although all compounds were colorless and the formation of a charge transfer complex between MV^{2+} and a neutral guest in the clathrates was not confirmed from the structural data and diffuse reflectance spectra, some of them showed a color change from colorless to blue on UV irradiation, and which arose from the reduction of MV^{2+} to a methylviologen radical MV^{+} .

VIII-R-2 IR Absorption Spectra of Electrochromic WO_3 Films

KONOSHIMA, Koji¹; GOTO, Takeshi; ISHIDA, Toshimasa¹; URABE, Kazuo¹; KITAO, Michihiko¹
(¹Shizuoka Univ.)

[*Trans. Mater. Res. Soc. Jpn.* 27, 349 (2002)]

WO_3 films were prepared by thermal evaporation. IR absorption spectra of the films were measured for

various amount of injected protons. Three peaks of $\nu(W-OH)$, $\nu(W=O)$ and $\nu(O-W-O)$ vibrations were observed. With increasing of injected protons, the intensity of peak of $\nu(W-OH)$ increased and its position shifted hugely from 3200 to 2400 cm^{-1} . We calculated various bond-patterns of OH vibrations. Then OH vibrations accompanied with hydrogen bonds are plausible for observed OH peaks. On the other hand, with increasing of injected protons the intensity of peak of $\nu(W=O)$ bond also increased, but its position shifted a little. It is considered that parts of $W-O-W-O-W$ bonds were broken by injected protons and then $W=O$ bonds were brought about.

VIII-R-3 A Local Interpolation Scheme Using No Derivatives in Potential Sampling: Application to $O(^1D) + H_2$ System

ISHIDA, Toshimasa; SCHATZ, George C.¹
(¹Northwestern Univ.)

[*J. Comput. Chem.* submitted]

We recently proposed a local interpolation scheme, in which interpolant moving least squares (IMLS) and Shepard interpolation are employed to describe potential energy surfaces. This IMLS/Shepard scheme is applicable to do potential interpolation with quantum chemical results for which analytical derivatives are not available. In this study, we apply the scheme to the highly exothermic $O(^1D) + H_2 \rightarrow H + OH$ reaction and compare it with results based on Shepard interpolation using second order Taylor expansions. An analytical surface is used to define the potential function so that errors in the interpolation function may accurately be determined. We found that the present scheme reproduces the correct reactive cross sections more accurately than the Shepard scheme, and with rms errors for energy and gradients that are significantly smaller than those from Shepard interpolation. This occurs even though the present scheme does not utilize derivative and hessian information whereas the Shepard interpolation does. The Bayesian approach proposed by Bettens and Collins does not improve the IMLS/Shepard results significantly although it does the Shepard-only approach. The accuracy in the IMLS/Shepard scheme is surprising, but can be explained by the more global nature of the interpolation.

VIII-R-4 Theoretical Study on Photoinduced Color Change and Charge Transfer of Methylviologen

ISHIDA, Toshimasa; MURAKAMI, Makoto¹;

WATANABE, Go¹; YOSHIKAWA, Hirofumi²;
NISHIKIORI, Shin-ichi²
(¹Shizuoka Univ.; ²Univ. Tokyo)

[*Internet Electron. J. Mol. Des.* submitted]

Motivation. Methylviologen dication is easily reduced to be a monocation radical, and turned to be blue, and forms a charge-transfer complex with a donor molecule. Yoshikawa *et al.* recently reported photo-induced reduction and charge transfer complexes in polycyanopolycadmate host clathrates. We study the reduction using quantum chemical calculations. The energy changes with the torsion angle of the two cations and the spectral change, solvent effect and the charge transfer between the dication and other guest molecules in the clathrates are investigated.

Method. The Hartree-Fock and CI singles, time dependent DFT calculations are carried out for the ground state and excited states of the two cations. Solvation effect is treated with the polarizable continuum model, and the charge transfer in the clathrates is modeled based on crystal structures determined experimentally.

Results. The optimized geometry of the monocation radical was found to be planar while that of the dication is twisted. These results are consistent with recent calculations for related compounds. The color change upon the photoreduction was reproduced by the calculation. The solvent effect of acetonitrile was found to be small. Charge transfer absorption was reproduced for the mesitylene-methylviologen dication complex in the clathrate host using a small model.

Conclusions. The geometrical and the color change was reproduced satisfactorily. The TDDFT scheme reproduces the observed spectra better than the CIS scheme, but the latter scheme is still valuable to evaluate qualitative feature of spectra.

VIII-R-5 Potential Energy Surface Generation Using Ab Initio Calculations and IMLS/Shepard Interpolation for the $\text{LiH} + \text{H} \rightleftharpoons \text{Li} + \text{H}_2$ Reactions

KIM, Kyoung Hoon¹; LEE, Yoon Sup¹; JEUNG, Gwang-Hi²; ISHIDA, Toshimasa³
(¹Korea Adv. Inst. Sci. Tech.; ²Univ. Paris-Sud;
³Shizuoka Univ.)

[*J. Chem. Phys.* submitted]

CASSCF following MRCI calculations are employed to generate potential energy surfaces for the reaction of $\text{LiH} + \text{H} \rightleftharpoons \text{Li} + \text{H}_2$ and analyze the reactive region for the reaction. Spectroscopic data for LiH and H_2 obtained by our scheme are in good agreement with experiment results. IMLS combined with Shepard interpolation method is used to interpolate the Potential energy surfaces. Trajectory calculations for $\text{LiH} + \text{H} \rightarrow \text{Li} + \text{H}_2$ on the interpolated potential energy surface illustrate that the initial vibrational content of LiH plays a rather minor role which is explained by the fact there is no energy barrier for the reaction $\text{LiH} + \text{H} \rightarrow \text{Li} + \text{H}_2$, and the reactive cross section has maximum value, when the initial collision energy is about 0.1 eV. Trajec-

tory calculations for $\text{Li} + \text{H}_2 \rightarrow \text{LiH} + \text{H}$ show that the reaction requires highly excited $\text{H}_2(v \geq 4)$ molecules for it to occur at low collision energy and it is more efficient to put the same amount energy into the H_2 vibration energy rather than translational energy.

VIII-S Macromolecular Self-Assembly Opens a Way to the Development of Novel Materials that Have Characteristics of Cellular Systems

In cellular systems, assembly of devices (*e.g.* enzymes) into complexes is a principle to construct supramolecular apparatuses and ensure the specificity, fidelity, and efficiency of intracellular events. Exchangeability of the components of the complex is also advantageous for adaptation to the environment and metabolism of the apparatus. For global, sustainable development, in our opinion, readiness for the adaptation and decomposition is required for any future materials and systems such as highly integrated device arrays. Utilizing elaborate macromolecular self-assemblies, we thus aimed at development of artificial systems endowed with energy- and entropy-saving properties: the system can be formed and function on demand, and are readily reusable, repairable, and bio-degradable. We attempt to fabricate the nano-systems for energy conversion and computing; for their basis, we also study on molecular mechanisms of photosynthesis and signal transduction. Our study should serve a new design concept for nano- and molecular-scale intelligent materials (see also Special Research Project (c)).

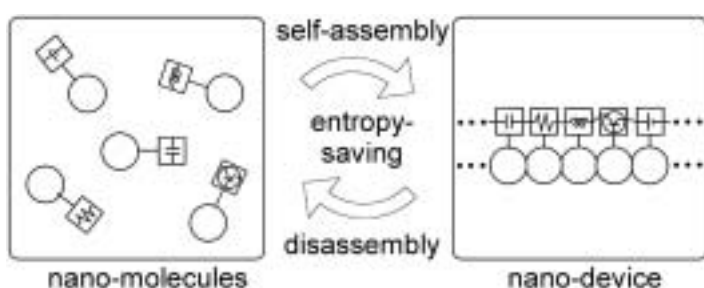


Figure 1. A concept of the “entropy-saving” nano-materials.

VIII-S-1 Fabrication of “Entropy-Saving” Nano-Solar-Cells

OBA, Toru; HANASAKI, Mitsuru¹; MINABE, Masahiro¹
(¹Utsunomiya Univ.)

Photosynthetic apparatuses in living organisms are, in common, assemblies of light-harvesting antenna parts and reaction centers (RCs) where energy conversion occur. Nano-scale order in the assembled supramolecular structure contributes efficient function. The assembly is advantageous to light adaptation and metabolism. These facts suggest that elaborate self-assembly of macromolecular components can provide solar-cells that can be formed and function on demand. We developed such device utilizing cytoskeletal nano-tubes, “microtubules” (MTs). The component protein “tubulin” (Tub) molecules assemble to form MTs at 37 °C in the presence of nucleotide, and MTs disassemble to Tubs at 0 °C. We prepared Tubs conjugated with a fluorophore for the antenna part and a photosensitizer-labeled hemoprotein for the RC, respectively. The modified Tubs were mixed and the temperature of the solution was switched simply. Only in the Tub-assembled state (MTs), solar energy absorbed by the antenna parts migrated to the sensitizer, leading to charge separation in the RC, as occurs in photosynthesis. The device reversibly functioned at each Tub-assembled state in the course of the Tub-assembly / MT-disassembly cycles.

VIII-S-2 Model Study on Signaling Behaviors of Scaffold Proteins—Toward its Application to Novel Computing Devices—

OBA, Toru; FUJIWARA, Umihito¹; MINABE, Masahiro¹
(¹Utsunomiya Univ.)

Scaffold proteins, found in postsynaptic termini, can bind several members of a signaling cascade to form a supramolecular complex, which may contribute to rapidity, fidelity, and selectivity of signal transduction.¹⁾ Such a mechanism can correlate to learning and memory formation. Due to the limitation of the experiments, however, no detailed model of scaffold action has been reported except for numerical simulations. We utilized a eukaryotic cytoskeleton ‘microtubule’ (MT) for fabrication of a model of the signaling complexes. We conjugated both glucose oxidase (GOx) and horseradish peroxidase (HRP) on the surface of an MT by use of the avidin-biotin interaction. The upstream effector (GOx) converted an input signal (*D*-glucose) into a second messenger (H₂O₂) that was diffusely supplied to the downstream effector (HRP) and converted into an output signal (Dye). It was found that sensitivity of the system to the stimulus increased with increasing density of the effectors on a MT. Further examinations of this model system may contribute to development of novel computing devices.

Reference

- 1) U. Thomas, “Modulation of synaptic signalling complexes by Homer proteins,” *J. Neurochem.* **81**, 407 (2002).

VIII-S-3 Physicochemical Studies on the Molecular Mechanism of Photosynthesis

OBA, Toru; TAMIYAKI, Hitoshi¹

(¹Ritsumeikan Univ.)

[*Photosynth. Res.* in press]

Since chlorophyll *a* and bacteriochlorophyll *a* are asymmetric molecules (Figure 1), an external ligand can coordinate to the central Mg atom either from the chlorin macrocycle side where the C13²-methoxycarbonyl moiety protrudes (denoting as the 'back' side) or from the other side (the 'face' side). We investigated which side of the macrocycle is favored for the ligand coordination, by survey of the highly resolved crystal structures of various photosynthetic proteins and theoretical model calculations. It is found that chlorophyll *a* as well as bacteriochlorophylls *a* and *b* in the photosynthetic proteins mostly bind their ligands on the 'back' sides. This finding was confirmed by the theoretical calculations for methyl chlorophyllide *a* and methyl bacteriochlorophyllide *a* as models: the 'back' type ligand-(bacterio)chlorophyll complex was more stable than the 'face' type one. The calculations predicted influence of the C13²-stereochemistry on the choice of the side of the ligand coordination, which may be correlated to the presence of the C13²-epimer of chlorophyll *a* in photosystem I reaction center.¹⁾

Reference

- 1) P. Jordan, P. Fromme, H. T. Witt, O. Klukas, W. Saenger and N. Krauß, "Three-dimensional structure of cyanobacterial photosystem I at 2.5 Å resolution," *Nature* **411**, 909 (2001).

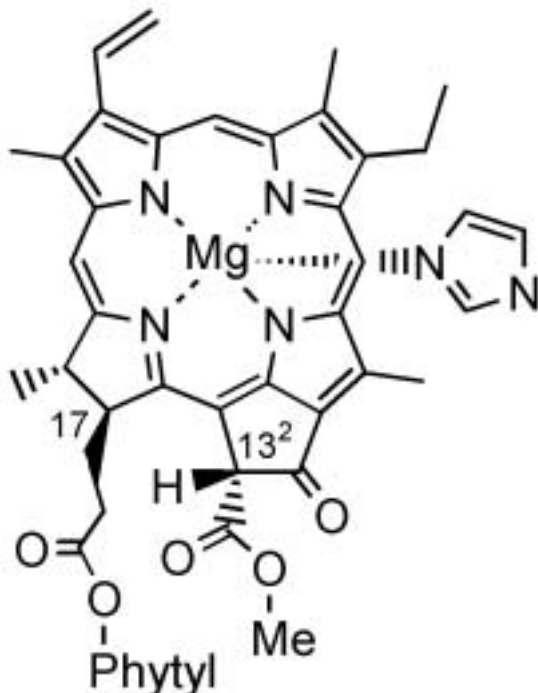


Figure 1. Molecular structure of the 'back' type chlorophyll *a*-imidazole complex.